



**HAL**  
open science

## A virtual chemical mechanism for prediction of NO emissions from flames

Giampaolo Maio, Mélody Cailler, Alberto Cuoci, Benoît Fiorina

► **To cite this version:**

Giampaolo Maio, Mélody Cailler, Alberto Cuoci, Benoît Fiorina. A virtual chemical mechanism for prediction of NO emissions from flames. *Combustion Theory and Modelling*, 2020, 24 (5), pp.872-902. 10.1080/13647830.2020.1772509 . hal-03419970

**HAL Id: hal-03419970**

**<https://hal.science/hal-03419970>**

Submitted on 8 Nov 2021

**HAL** is a multi-disciplinary open access archive for the deposit and dissemination of scientific research documents, whether they are published or not. The documents may come from teaching and research institutions in France or abroad, or from public or private research centers.

L'archive ouverte pluridisciplinaire **HAL**, est destinée au dépôt et à la diffusion de documents scientifiques de niveau recherche, publiés ou non, émanant des établissements d'enseignement et de recherche français ou étrangers, des laboratoires publics ou privés.

## A virtual chemical mechanism for prediction of NO emissions from flames

G. Maio<sup>a</sup>, M. Cailler<sup>b</sup>, A. Cuoci<sup>c</sup> and B. Fiorina<sup>a</sup>

<sup>a</sup>Laboratoire EM2C, CNRS, CentraleSupélec, Université Paris-Saclay, 3 rue Joliot Curie 91192 Gif Sur Yvette cedex, France

<sup>b</sup>SAFRAN Tech, Rue des Jeunes Bois, Châteaufort - CS 80112, 78772 Magny-les-Hameaux, France

<sup>c</sup>Department of Chemistry, Materials and Chemical Engineering "G. Natta", Politecnico di Milano, Milano 20133, Italy

### ARTICLE HISTORY

Compiled May 17, 2020

### ABSTRACT

A reduced order kinetic model for NO (Nitric Oxide) prediction, based on the virtual chemistry methodology [1], is developed and applied. Virtual chemistry aims to optimize thermochemical properties and kinetic rate parameters of a network of virtual species and reactions. A virtual main chemical mechanism is dedicated to temperature and heat release prediction and is coupled with the flow governing equations, whereas satellite sub-mechanisms are designed to predict pollutants formation. Two virtual chemistry mechanisms are here employed: a main mechanism for calculating the temperature and heat release rate and a second mechanism dedicated to NO prediction. To recover the chemical structure of multi-mode combustion, both premixed and non-premixed flamelets are included in the learning database used to optimize the virtual NO mechanism. A multi-zone optimization procedure is developed to accurately capture both fast and slow NO chemistry that include prompt, thermal and reburning pathways. The proposed NO sub-mechanism and optimization methodology are applied to CH<sub>4</sub>/air combustion. Laminar 1-D premixed and non-premixed flamelet configurations are first tested. The approach is then further assessed in 2-D CFD laminar flame simulations, by providing a direct comparison against detailed chemistry. 2-D premixed, non-premixed and partially premixed flame configurations are numerically investigated. For all cases, the virtual mechanism fairly captures temperature and NO<sub>x</sub> chemistry with only 12 virtual species and 8 virtual reactions with a drastic CPU time reduction compared to detailed chemistry.

### KEYWORDS

Nitric oxide ; virtual chemistry ; laminar flames ; reduced chemistry

## 1 Introduction

Nitrogen oxides (NO<sub>x</sub>) emitted in the atmosphere, even in small quantities, cause problems to the local air quality. They contribute to acid rain, ozone production and smog formation. Combustion processes are the main source of nitrogen oxides emissions [2]. To limit their production engineers need numerical tools to design and optimize

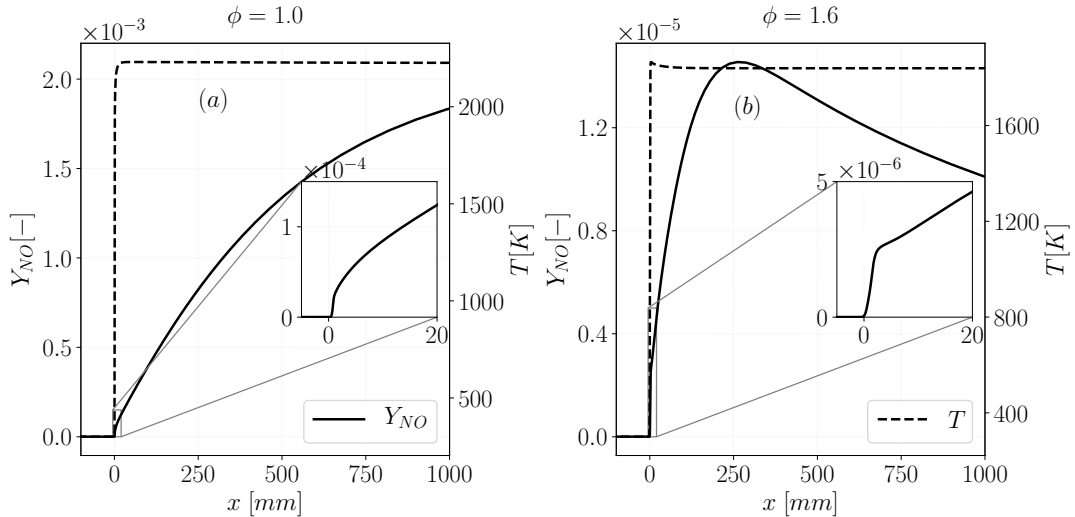


Figure 1.: Temperature and NO mass fraction profiles from CH<sub>4</sub>/air 1-D premixed flames computed at two different equivalence ratios (stoichiometric and rich) with the GRI3.0 mechanism [3]. Pressure is equal to 1 atm and the initial temperature equals 300K. The computational domain covers 1 m and includes the flame front and post-flame regions. The inner zoom plots show the NO mass fraction with a domain length comparable with the flame thermal thickness.

6 combustion devices. The numerical prediction of NO<sub>x</sub> emission is a challenging task  
7 for three main reasons: *i*) NO<sub>x</sub> are produced in very small quantities; *ii*) NO<sub>x</sub> for-  
8 mation and consumption feature multiple chemical time scales and *iii*) NO<sub>x</sub> chemical  
9 paths vary with the operating conditions (fuel, temperature, pressure, equivalence ra-  
10 tio, etc.). At the combustion chamber exit, NO<sub>x</sub> are mainly composed of NO [4], whose  
11 chemistry complexity is well illustrated in Fig. 1. The detailed chemistry solutions of  
12 stoichiometric and rich ( $\phi = 1.6$ ) premixed 1-D freely propagating laminar flames,  
13 obtained using REGATH solver [5] and GRI3.0 detailed mechanism [3] for CH<sub>4</sub>/air  
14 combustion, are shown. A thin flame front region zone, of the order of the millimeter,  
15 is first identified within the thermal flame thickness. NO chemistry has here a char-  
16 acteristic time scale comparable to the fuel oxidation process. The chemical pathway,  
17 leading to this flame front NO formation, is identified as *prompt* route [6, 7]. A second  
18 zone is observed in the post-flame region where temperature and major species reach  
19 chemical equilibrium, while NO mass fraction still evolves slowly. Furthermore, in the  
20 post-flame zone, NO chemistry exhibits two different behaviours:

- 21 • For lean, stoichiometric and moderately rich conditions: a slow, monotonic, NO  
22 production is observed until the chemical equilibrium is reached. This process is  
23 mainly governed by the *thermal* [8] route.
- 24 • For very rich conditions ( $\phi \geq 1.4$ ): the slow NO formation competes with NO  
25 recombination [9] causing a non-monotonic evolution of NO mass fraction. The  
26 NO consumption is known as *reburning* process [10, 11].

27 Detailed chemistry mechanisms currently include and combine *prompt*, *thermal* and  
28 *reburning* pathways, to describe NO formation in as many as possible flame conditions  
29 [12]. However hydrocarbons detailed chemical mechanisms involve hundreds of species

30 and reactions [13] and their size further increase with the consideration of NO chem-  
31 istry. For example in the GRI3.0 mechanism [3], widely used to describe CH<sub>4</sub> oxidation,  
32 the NO<sub>x</sub> chemistry subset adds 17 species and 108 reactions to the initial mechanism  
33 made of 36 species and 217 reactions. As direct inclusion of detailed chemistry in CFD  
34 simulations causes CPU cost issues, reduced order models are needed to mitigate the  
35 computational burden [14, 13, 15]. Three main modeling strategies are currently em-  
36 ployed in the literature to model combustion chemistry at reduced CPU cost [15, 16]:  
37 global mechanisms [17, 18], tabulated chemistry [19, 20, 21] and analytically reduced  
38 chemistry [22, 23].

39 A widely used technique to capture main combustion chemistry properties is to  
40 develop and optimize empirical global and semi-global mechanisms [24, 25], containing  
41 from 1 to 4 reaction steps. Unfortunately these mechanisms are not suitable to predict  
42 NO because, including only a few number of species, they do not contain NO chemistry  
43 species.

44 An alternative strategy is the systematic reduction of detailed mechanisms. Analyti-  
45 cally reduced mechanisms [13] have been especially developed to capture NO formation  
46 [26]. This strategy allows to predict NO formation [22] over multiple flame regimes  
47 with an acceptable error. However, the application of analytically reduced mechanism  
48 to large scale simulations [26, 27] is still CPU demanding.

49 The last standard route for chemistry reduction is the “tabulated chemistry” for-  
50 malism [19, 28]. It aims at pre-computing, in a preliminary step, the reduced manifold  
51 in which the chemical subspace evolves. The manifold is finally coupled with a CFD  
52 solver to model the combustion process. In flamelet based tabulated chemistry meth-  
53 ods, all detailed chemistry ingredients are included within a chemical table build-up  
54 from a collection of 0-D reactors or 1-D flame archetypes [20, 21, 29]. The defini-  
55 tion and the coordinates of the chemical database depend on the complexity of the  
56 targeted computed flame regime. In the literature, the potential of tabulated chem-  
57 istry for NO formation prediction has been investigated first by Nafe and Mass [30].  
58 Analysing PSRs (Perfectly Stirred Reactors) solutions, using the ILDM (Intrinsic Low-  
59 Dimensional Manifolds) [28] approach, they conclude that additional slow time scales  
60 associated with NO chemistry exist. In the flamelet framework one strategy, to model  
61 NO formation, is to include nitrogen species in the progress variable definition and to  
62 add a dedicated transport equation for NO mass fraction in the flow solver [31, 32].  
63 Another strategy, originally developed in the FPV formalism (flamelet/progress vari-  
64 able) [33] and then adapted to the FGM model (flamelet generated manifolds) [34],  
65 consists in splitting the NO chemical source term in a production and a consump-  
66 tion contributions and in adding an additional transport equation for the NO mass  
67 fraction in the flow solver. An original tabulated chemistry approach, called NOMANI  
68 model, has been proposed by Pecquery *et al.* in the FPI (Flame prolongation of ILDM)  
69 context [35]. In the NOMANI model, the NO source term is split in a flame front con-  
70 tribution and in a burnt gases contribution which are extracted from two separate  
71 look-up tables (carbon and nitrogen), parametrised from two different progress vari-  
72 ables. The NORA model (NO Relaxation Approach) [36], dedicated to thermal NO  
73 prediction in internal combustion engines, is another example of tabulated chemistry  
74 application to NO prediction using a collection of PSRs solutions. However particular  
75 attention is required when NO mass fraction is retained as a progress variable in the  
76 post-flame region. As shown in Fig 1b, in rich conditions, NO mass fraction is not  
77 strictly monotonous and cannot be considered as progress variable. Godel *et al.* [31]  
78 overcame this limitation, by using an optimized combination of N-species to build-up  
79 an appropriate NO chemistry progress variable valid also for rich conditions.

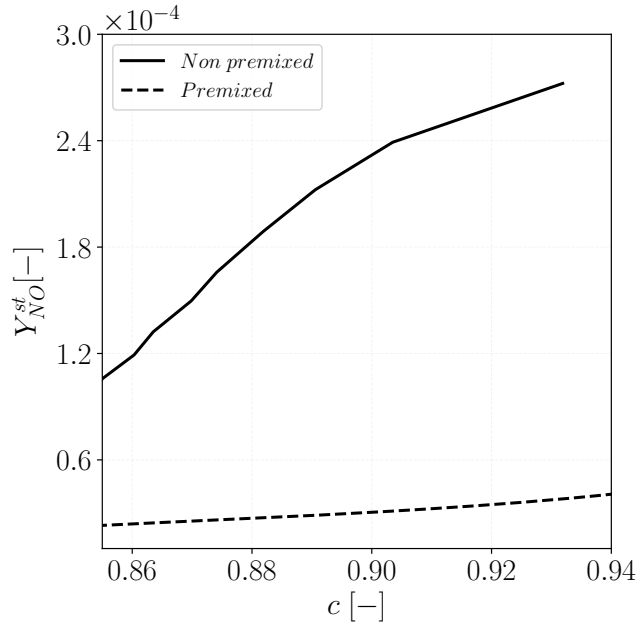


Figure 2.: NO mass fraction flamelet trajectories for a  $\text{CH}_4/\text{air}$  mixture, at atmospheric pressure and initial temperature of 300K, computed with GRI3.0 mechanism [3]. The data are plotted as a function of progress variable ( $c$ ) over the stoichiometric mixture fraction ( $Z_{st}$ ) cut-plane. Data are extracted from a premixed and a non-premixed database.

80 Despite the extensive and successful applications, tabulated chemistry fails when the  
 81 local flame structure differs from the tabulated archetype [37, 38, 39]. As an example,  
 82 Fig. 2 shows the trajectories projection in the  $Y_{NO}$ -progress variable ( $c$ ) sub-space  
 83 over the stoichiometric cut-plane ( $Z = Z_{st}$ ), of both premixed and non-premixed 1-D  
 84 flamelets. The 1-D flames are computed using REGATH solver [5] and GRI3.0 detailed  
 85 mechanism [3] for  $\text{CH}_4/\text{air}$  mixture. The NO mass fraction trajectories show signifi-  
 86 cant differences (up to an order of magnitude) between the two databases for the same  
 87 mixture fraction ( $Z_{st}$ ) and the same progress variable ( $c$ ) values. This demonstrates  
 88 that tabulated chemistry, does not perform well for NO formation in multi-mode com-  
 89 bustion, if a single flame regime is accounted in the database generation.

90 An alternative reduction chemistry route, named *virtual chemistry*, has been re-  
 91 cently developed by Cailler *et al.* [40]. The method consists in building-up empiri-  
 92 cal mechanisms made of virtual species and reactions. As in tabulated chemistry, an  
 93 ensemble of reference flame archetypes is first computed. However instead of "tab-  
 94 ulating" low-dimensional manifolds, thermodynamic and chemical properties of the  
 95 virtual components are optimized to fit an ensemble of targeted flame solutions. It  
 96 has been observed by Cailler *et al.* [1] that multi-mode combustion regimes are well  
 97 captured with a limited number of virtual species and virtual reactions as soon as both  
 98 premixed and non-premixed flame elements are included in the learning database. CO  
 99 emissions have been accurately predicted in a turbulent confined aeronautical combus-  
 100 tor exposed to heat losses [41]. Virtual chemistry is then a good candidate to model  
 101 NO formation in hybrid flame structures.

102 The objective of the present study is to propose a new reduced mechanism in the

103 virtual chemistry formalism able to predict NO in hybrid combustion regimes. The  
 104 challenge is to account for all the NO chemistry pathways, included in detailed chem-  
 105 istry for premixed and non-premixed flames. In section 2, the NO mechanism is intro-  
 106 duced whereas the optimization strategy and the application to CH<sub>4</sub>/air combustion  
 107 are described in section 3. Section 4 shows and discusses the validation results in 1-D  
 108 premixed freely propagating flames and in non-premixed counterflow flames, compar-  
 109 ing the virtual chemistry results against simulations carried out with the detailed  
 110 kinetic mechanism. In section 5, the proposed mechanism is further assessed in 2-D  
 111 CFD laminar flame simulations, employing the open source solver laminarSMOKE  
 112 [42]. A premixed, a non-premixed and a partially premixed flame configuration are  
 113 studied.

## 114 2. Virtual mechanism architecture

### 115 2.1. Virtual chemistry concept

116 A virtual chemical scheme is made of an ensemble of optimized mechanisms dedicated  
 117 to predict user-defined flame properties. Quantities of interest might be the heat re-  
 118 lease and the temperature [40] or the formation of some pollutants such as for instance  
 carbon monoxide [1, 41] or nitrogen oxides.

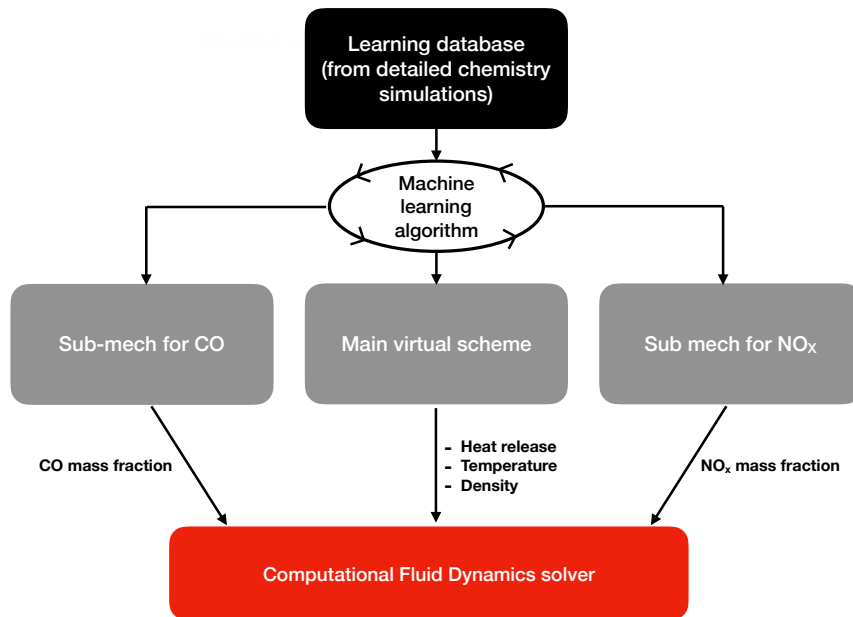


Figure 3.: Schematic representation of the virtual chemistry methodology. In this example the virtual scheme is made of a main mechanism dedicated to predict the heat release, temperature and density and two sub-mechanisms designed to model the formation of CO and NO<sub>X</sub>, respectively.

119 The general methodology to design and optimize a virtual chemical scheme is schematized in Fig. 3. A learning database is first built-up from detailed chemistry solutions of canonical flame archetypes. A main mechanism composed of virtual species and reactions is then designed and trained through a machine learning algorithm to target the thermal flame structures given by the learning database. More precisely, the main

125 virtual scheme models the reactive mixture thermodynamic and transport properties  
 126 as well as the heat released by combustion. The main mechanism is then implemented  
 127 in a CFD flow solver through the mass, momentum and energy equations.

128 Detailed chemistry ingredients are accounted for during the optimization stage of  
 129 the main mechanism but, as integrated flame quantities (flame speed, heat release,  
 130 etc.) and temperature are targeted, individual species information are not accessible  
 131 anymore. Independent satellite virtual sub-mechanisms are designed and optimized  
 132 to access specific species mass fractions of interest. As an example, a virtual sub-  
 133 mechanism dedicated to CO prediction has been developed in [1] and applied to a  
 134 turbulent flame LES in [41].

135 This section proposes a virtual chemical scheme architecture for NO prediction.  
 136 The virtual chemistry mathematical formalism is first presented in section 2.2 and a  
 137 main virtual mechanism adequate for hydrocarbon-air combustion is then reviewed in  
 138 section 2.3. A NO virtual sub-mechanism is proposed and discussed in section 2.4.

## 139 2.2. Virtual chemistry formalism

140 A virtual scheme  $X$  includes  $N_s$  virtual species and  $N_r$  virtual reactions, where  $X$   
 141 denotes either the main mechanism or a sub-mechanism. Any virtual mechanism  $X$  is  
 142 composed by an ensemble of reversible virtual reactions  $R_i^X$ :



143 where  $N_s^i$  is the number of virtual species involved in the virtual reaction  $R_i^X$ .  $\nu_k$   
 144 denotes the  $k^{th}$  virtual species whereas  $\alpha'_{ki}$  and  $\alpha''_{ki}$  are the reactant and product mass  
 145 stoichiometric coefficients, respectively. The reaction progress  $q_i$ , for the reaction  $R_i^X$ ,  
 146 is closed using a finite rate formulation with modified reaction orders:

$$q_i = k_{fi} \prod_{k=1}^{N_s} [\nu_k]^{F_k^i} - k_{bi} \prod_{k=1}^{N_s} [\nu_k]^{B_k^i} \quad (1)$$

147 where  $[\nu_k]$  is the  $k^{th}$  molar species concentration,  $F_k^i$  and  $B_k^i$  are the forward and  
 148 backward reaction orders corresponding to the  $k^{th}$  species in the  $i^{th}$  reaction.  $k_{fi}$  and  
 149  $k_{bi}$  are the forward and backward rate constants.  $k_{fi}$  is expressed using an Arrhenius-  
 150 like formulation:

$$k_{fi} = A_i T^{\beta_i} \exp\left(\frac{-E_a^i}{RT}\right) \quad (2)$$

151 where  $A_i$  is the pre-exponential factor,  $E_a^i$  is the activation energy and in the modified  
 152 Arrhenius law a temperature exponent  $\beta_i$  is added. When  $R_i^X$  is a reversible reaction,  
 153 the backward rate constant is related to the forward one through the following relation:

$$k_{bi} = \frac{k_{fi}}{K_{eq,i}} \quad (3)$$

154 with  $K_{eq,i}$  the equilibrium constant of reaction  $R_i^X$  defined as:

$$K_{eq,i} = \prod_{k=1}^{N_s^i} ([\nu_k]^{eq})^{\alpha''_{ki} - \alpha'_{ki}} \quad (4)$$

155 where  $[\nu_k]^{eq}$  is the targeted equilibrium concentration of species  $\nu_k$ .

156

157 The kinetic rate parameters of virtual reactions in the virtual mechanism  $X$   
 158 are optimized through the evolutionary algorithm proposed by Cailler *et al.* [40]. The  
 159 optimization problem consists in minimizing the following cost function  $C$  which aims  
 160 to compare the virtual and detailed chemistry solutions through a linear combination  
 161 of selected normalized flame quantities:

$$C = f\left(\mathbf{w}^v(\chi^v), \mathbf{w}^d(\chi^d)\right) \quad (5)$$

162 where the vector  $\mathbf{w} = (\rho u, \rho v, \rho w, \rho Y_k, T)$  is the solution of the system of flow gov-  
 163 erning equations, which depends on the set of parameters  $\chi$ . The vector  $\chi$  includes  
 164 the set of thermodynamic, transport and kinetic rate parameters.  $^d$  and  $^v$  superscripts  
 165 refer to detailed and virtual chemistry, respectively.  $\chi^d$  is given by the complex ther-  
 166 modynamic and transport properties and by the detailed chemical scheme involved  
 167 to build-up the learning database.  $\chi^v$  is the set of thermo-chemistry and transport  
 168 parameters to optimize, which constitutes the output of the optimization procedure.

### 169 **2.3. Main mechanism**

170 Different forms of virtual mechanism have been tested to recover the thermal flame  
 171 structure of a learning database composed of both premixed and non-premixed  
 172 flamelets. Tests performed in [40] showed that one-step chemical schemes does not  
 173 have enough degrees of freedom to handle both fast exothermic and slow endothermic  
 174 CO reactions observed under rich conditions. On the contrary a virtual mechanism  
 175 made of two consecutive reactions accurately capture the thermal flame structure of  
 176 both premixed and diffusion flames. The following 2-step main virtual mechanism is  
 177 therefore retained:



178 where  $\alpha_k^{X,i}$  are stoichiometric coefficients per mass unit. Fuel (F) and oxidizer (Ox) are  
 179 transformed through reaction  $R_1^T$  in an intermediate species (I) which is then converted  
 180 by reaction  $R_2^T$  into  $N_P^v$  virtual products  $P_k$ . Extensive tests conducted in [40] showed  
 181 that an accurate prediction of equilibrium flame temperature over the whole range of  
 182 equivalence ratio is obtained with  $N_P^v = 4$ .

183 The reaction progresses of the two irreversible reactions  $R_1^T$  and  $R_2^T$  are closed with  
 184 extended Arrhenius formulation as follows:



$$q_1^T = A_1^T(Z) \exp\left(\frac{-E_a^{T,1}}{RT}\right) [F]^{F_F^{T,1}} [O]^{F_{O_x}^{T,1}} \quad (6)$$

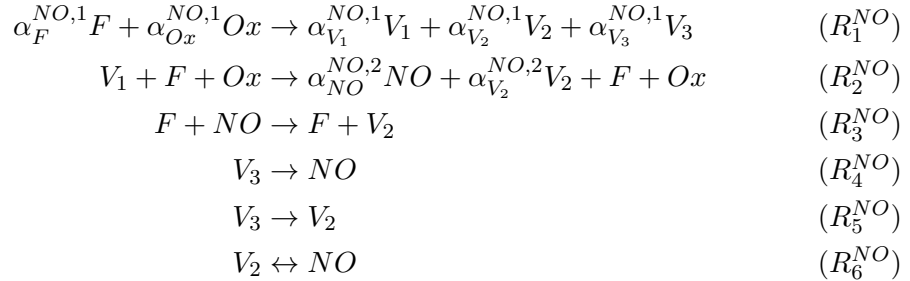
$$q_2^T = A_2^T \exp\left(\frac{-E_a^{T,2}}{RT}\right) [I]^{F_I^{T,2}(Z)} \quad (7)$$

185 Contrary to standard Arrhenius formulations, the pre-exponential constant of Eq. 6  
 186 and the reaction order  $F_I^{T,2}(Z)$  are expressed as dependent on the mixture fraction  $Z$ ,  
 187 and calibrated to match the laminar flame speed and thickness within the flammability  
 188 limits [40]. As preferential species diffusion is not accounted for, the mixture fraction  
 189 is given by the solution of an additional passive scalar balance equation [15].

190 Thermodynamic and transport properties of the virtual species as well as specific  
 191 gas constants are calibrated to recover averaged properties of the multi-component  
 192 real mixture. In addition, equilibrium constants are defined to retrieve real equilib-  
 193 rium compositions. For the sake of conciseness, details of virtual species thermo-  
 194 dynamics properties are not given here, but we encourage the reader to refer to [1]  
 195 for further details. The next section is dedicated to the description of the virtual NO  
 196 sub-mechanism, which constitutes the main novelty of this work.

#### 197 **2.4. NO mechanism**

198 A mechanism architecture is proposed to account for the whole NO chemical pathways  
 199 evidenced previously in Fig. 1: *prompt*, *thermal* and *reburning*. For that purpose, the  
 200 following NO virtual sub-mechanism, composed of 6 reactions, is proposed:



201 where  $\alpha_k^{NO,i}$  are the mass stoichiometric coefficients associated to species  $k$  in the  
 202 reaction  $R_i$ . An ensemble of virtual species  $V_1$ ,  $V_2$  and  $V_3$  is first produced through the  
 203 initiation reaction  $R_1^{NO}$ . Note that unlike to “real” mechanism, element conservation  
 204 is not required in virtual reactions as intermediate species  $V_1$ ,  $V_2$  and  $V_3$  does not  
 205 have any physical representation, but represent degrees of freedom of the model.

206 Reactions  $R_2^{NO}$  and  $R_3^{NO}$  are dedicated to model the fast NO chemistry, which is  
 207 dominant at the flame front scale.  $R_3^{NO}$  is designed to reproduce the fast NO reburning  
 208 that is especially relevant when an excess of hydrocarbon radicals is present in the  
 209 system [11]. In addition, as it will be shown in section 4.3, using two reactions ( $R_2^{NO}$ -  
 210  $R_3^{NO}$ ) to model fast NO formation, instead of one ( $R_2^{NO}$ ), enables a better prediction of  
 211 both premixed and non-premixed NO profiles. Virtual reactions  $R_4^{NO}$  to  $R_6^{NO}$  describe  
 212 the NO formation associated with slow post-flame chemistry. It includes thermal NO

213 pathway and slow NO reburning phenomena. As discussed later in section 4.2, the  
 214 combination of three reactions allows an efficient description of slow NO post-flame  
 215 pathways in both lean and rich regimes. Finally, the equilibrium reaction  $R_6^{NO}$  ensures  
 216 that the chemical equilibrium conditions are well retrieved.

217 The rate of progress for the reactions set  $R_1^{NO}$ - $R_6^{NO}$  are closed using the following  
 218 Arrhenius-like expressions:

$$q_1^{NO} = A_1^{NO} (Z) \exp\left(\frac{-E_a^{NO,1}}{RT}\right) [F]^{F_F^{NO,1}} [O]^{F_{O_x}^{NO,1}} \quad (8)$$

$$q_2^{NO} = A_2^{NO} (Z) \exp\left(\frac{-E_a^{NO,2}}{RT}\right) T^{\beta_T^{NO,2}} [V_1]^{F_{V_1}^{NO,2}} [F] [Ox] \quad (9)$$

$$q_3^{NO} = A_3^{NO} \exp\left(\frac{-E_a^{NO,3}}{RT}\right) [F] [NO]^{F_{NO}^{NO,3}} \quad (10)$$

$$q_4^{NO} = A_4^{NO} (Z) \exp\left(\frac{-E_a^{NO,4}}{RT}\right) [V_3]^{F_{V_3}^{NO,4}} \quad (11)$$

$$q_5^{NO} = A_5^{NO} (Z) \exp\left(\frac{-E_a^{NO,5}}{RT}\right) [V_3]^{F_{V_3}^{NO,5}} \quad (12)$$

$$q_6^{NO} = A_6^{NO} (Z) \exp\left(\frac{-E_a^{NO,6}}{RT}\right) \left( [NO]^{F_{NO}^{NO,6}} [V_2]^{F_{V_2}^{NO,6}} - \frac{[NO]^{B_{NO}^{NO,6}} [V_2]^{B_{V_2}^{NO,6}}}{K_c^{NO,6}} \right) \quad (13)$$

219 The equilibrium constant for the reversible reaction  $R_6^{NO}$  is computed as follows:

$$K_c^{NO,6} = \frac{[NO]^{d|eq}}{[V_2]^{v|eq}} \quad (14)$$

220 where  $[NO]^{d|eq}$  is the equilibrium NO molar concentration obtained from detailed  
 221 equilibrium computations.  $[V_2]^{v|eq}$  is computed from the knowledge of  $V_2$  mass fraction  
 222 at equilibrium condition.

223 In “real” mechanisms, mass conservation implies that all species mass sums to one.  
 224 It is not the case for virtual chemistry, where mass conservation is satisfied separately,  
 225 by optimizing the mixture averaged molecular weight [40, 1], regardless of the sum of  
 226 the mass fractions of species. Constraints are however needed in practice to regularize  
 227 the optimization problem. By convention, the formalism retained imposes that each  
 228 set of species mass fractions which constitutes a virtual (main or sub) mechanism sum  
 229 to unity:

$$\sum_{k=1}^{N_s^X} Y_k = 1 \quad (15)$$

230 where  $N_s^X$  is the number of species contained in the virtual mechanism X. Conse-  
 231 quently,  $Y_{V_2}$  is computed from Eq. 15 with  $N_s^X = N_s^{NO}$  as:

$$Y_{V_2}|^{eq} = 1 - Y_F|^{eq} - Y_{Ox}|^{eq} - Y_{NO}|^{eq} - Y_D|^{eq} - Y_{V_1}|^{eq} - Y_{V_3}|^{eq} \quad (16)$$

232  $Y_{V_1}|^{eq}$  and  $Y_{V_3}|^{eq}$  are theoretically equal to zero at equilibrium since the species  $V_1$   
 233 and  $V_3$  are completely consumed through the reactions  $R_2^{NO}$ ,  $R_4^{NO}$  and  $R_5^{NO}$ .  $Y_F|^{eq}$ ,  
 234  $Y_{Ox}|^{eq}$  and  $Y_D|^{eq}$  are known quantities from the main virtual mechanism solution while  
 235  $Y_{NO}|^{eq}$  is assumed equal to the reference one. However, it has been noticed that for  
 236 very lean and rich conditions  $Y_{V_1} \neq 0$  at equilibrium. In the 2ZONE optimization,  
 237 detailed in section 3.3,  $Y_{V_1}|^{eq}$  will be a known quantity at the end of the flame-front  
 238 block optimization and it is easily accounted for in Eq. 16 for computing  $Y_{V_2}|^{eq}$ , before  
 239 performing the post-flame block optimization.

The reaction orders  $F_{V_1}^{NO,2}$ ,  $F_{NO}^{NO,3}$ ,  $F_{V_3}^{NO,4}$ ,  $F_{V_3}^{NO,5}$ ,  $F_{NO}^{NO,6}$  and  $F_{V_2}^{NO,6}$  involved in  
 forward reactions  $R_1^{NO}$  to  $R_6^{NO}$  are included in the set of optimized parameters. Under  
 equilibrium conditions, the net reaction rate  $q_6^{NO}$  equals zero. To satisfy this constraint,  
 reaction orders  $B_{NO}^{NO,6}$  and  $B_{V_2}^{NO,6}$  of backward reaction  $R_6^{NO}$  involved in Eq. 13 but  
 must satisfy the following relations [1] :

$$B_{NO}^{NO,6} = F_{NO}^{NO,6} + 1 \quad (17)$$

$$B_{V_2}^{NO,6} = F_{V_2}^{NO,6} - 1 \quad (18)$$

240 The set of kinetic rate parameters to optimize includes the pre-exponential constants  
 241  $A_i$  the activation energies  $E_a^i$ , forward reaction orders  $F_k^i$  and species stoichiometric  
 242 coefficients  $\alpha_k^i$  for reactions  $R_1^{NO}$  to  $R_6^{NO}$  and the temperature exponent  $\beta_T^{NO,2}$ .

243 To limit the number of transported species, the species F and Ox are identical  
 244 in both main and NO virtual mechanisms. Consequently, kinetic parameters of reac-  
 245 tions  $R_1^T$  and  $R_1^{NO}$  are identical:  $\alpha_F^{NO,1} = \alpha_F^{T,1}$ ;  $\alpha_{Ox}^{NO,1} = \alpha_F^{T,1}$ ;  $A_1^{NO} = A_1^T$ ;  $E_a^{NO,1} =$   
 246  $E_a^{T,1}$ ;  $F_{F,1}^{NO} = F_{T,1}^{NO}$  and  $F_{Ox,1}^{NO} = F_{T,1}^{Ox}$ .

247 To capture the sensitivity of NO reaction rate to the equivalence ratio, the optimized  
 248 pre-exponential constants  $A_2$ ,  $A_4$ ,  $A_5$  and  $A_6$  are tabulated as a function of the mixture  
 249 fraction  $Z$  with first-order interpolation.

250 Reactions  $R_4^{NO}$  and  $R_5^{NO}$  are needed to retrieve the slow NO formation and its  
 251 successive recombination characterizing rich flame conditions, as discussed in section  
 252 1. This phenomenon is observed in the NO detailed profiles starting from  $\phi = 1.4$ . In  
 253 practice, reactions  $R_4^{NO}$  and  $R_5^{NO}$  are activated for  $\phi \geq 1.4$  through the stoichiometric  
 254 coefficient  $\alpha_{V_3}^{NO,1}$ . Section 4.2 discusses the importance of adding reactions  $R_4^{NO}$  and  
 255  $R_5^{NO}$  for rich conditions. The following section 3 gives details about the optimization  
 256 procedure.

### 257 3. Optimization of the NO virtual scheme

#### 258 3.1. Principle

259 Figure 4 summarizes the general NO mechanism optimization procedure. The vector  
 260  $\chi^v$  contains the ensemble of selected kinetic rate parameters for the virtual NO sub-  
 261 mechanism, as discussed in the previous section.  $N$  random individuals, corresponding  
 262 to  $N$   $\chi_n^v$  vectors, evolve for a certain number of generations  $N_{gen}$ , in the optimization  
 263 loop, according to the evolutionary algorithm designed by Cailler *et al.* [40]. Each

264 parameter of the vector  $\chi_n^v$  may mutate in the genetic optimization loop within user-  
 265 defined lower and upper bounds. After a pre-defined number of genetic generations  
 $N_{gen}$ , the best individual (best  $\chi^v$  vector) is identified as output.

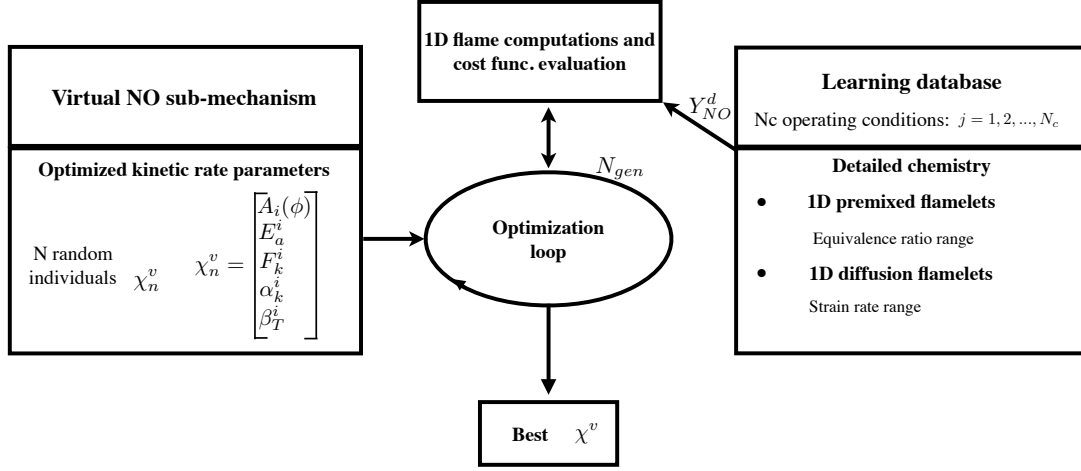


Figure 4.: Schematic view of the general procedure employed to optimize the kinetic rate parameters of the NO virtual mechanism.

266  
 267 As discussed in [1], to capture pollutant formation in multi-mode combustion, the  
 268 learning database must include information from both 1-D premixed flames and  
 269 1-D non-premixed counterflow flames. To account for these two different flamelet  
 270 archetypes, the cost function  $C_{NO}$  used in the optimization procedure is computed  
 271 as:

$$C_{NO} = C_{NO}^P + C_{NO}^{NP} \quad (19)$$

272 where  $C_{NO}^P$  and  $C_{NO}^{NP}$  are the cost functions relative to premixed flamelet library and  
 273 non-premixed one, respectively.  $C_{NO}^P$  is defined from the NO mass fraction as follows:

$$C_{NO}^P = \sum_{i=1}^{N_\phi} \frac{\|Y_{NO}^{P,v}(\phi_i^0) - Y_{NO}^{P,d}(\phi_i^0)\|_{L_2}}{\|Y_{NO}^{P,d}(\phi_i^0)\|_{L_2}} \quad (20)$$

274 where  $Y_{NO}^{P,v}$  and  $Y_{NO}^{P,d}$  are the NO mass fraction of a freely propagating premixed flame  
 275 computed with the virtual and detailed mechanism, respectively. The introduction of  
 276 the L2 norm  $\|\varphi\| = \sqrt{\int_{-\infty}^{+\infty} \varphi(x)^2 dx}$  provides a global flame criteria and avoid local  
 277 issues where  $Y_{NO}$  approaches zero.  $N_\phi$  is the number of premixed flamelets included  
 278 in the learning database.  $\phi_i^0$  is the fresh gases equivalence ratio of the  $i^{th}$  flamelet.  
 279  $x$  is the premixed flame coordinate normal to the flame front.  $x \in \mathcal{A}^P$ , where  $\mathcal{A}^P$   
 280 is the spatial subspace targeted during the optimization procedure for each premixed  
 281 flamelet. If the whole flame domain is targeted during the optimization process, then  
 282  $\mathcal{A}^P = [-\infty, +\infty]$ , where  $x = -\infty$  and  $x = +\infty$  correspond to fresh and burn gases  
 283 conditions, respectively.  
 284  $C_{NO}^{NP}$  is defined from the NO mass fraction maximum value along the non-premixed

285 flame domain:

$$C_{NO}^{NP} = \sum_{j=1}^{N_a} \frac{\max_y |Y_{NO}^{NP,v}(y, a_j)| - \max_y |Y_{NO}^{NP,d}(y, a_j)|}{\max_y |Y_{NO}^{NP,v}(y, a_j)|} \quad (21)$$

286 where  $Y_{NO}^{NP,v}$  and  $Y_{NO}^{NP,d}$  are the NO mass fraction of a non-premixed counterflow flame  
 287 computed with the virtual and detailed mechanism, respectively.  $N_a$  is the number of  
 288 non-premixed flamelets included in the learning database and  $a_j$  is the strain rate  
 289 of the  $j^{th}$  flamelet.  $a_j \in \mathcal{A}^{NP}$ , where  $\mathcal{A}^{NP} = \{a_0, a_{N_a}\}$  is the range of strain rates  
 290 targeted. If the whole ensemble of steady state non-premixed flamelets is considered,  
 291 then  $a_0 = 0 \text{ s}^{-1}$  and  $a_{N_a} = a_q$  where  $a_q$  is the strain rate at quenching.  $y$  is the  
 292 1-D flame coordinate. Two optimization strategies, based on 1 or 2 zones, are now  
 293 compared in the following sections.

### 294 **3.2. Single zone optimization (1ZONE)**

295 The 1-zone optimization (1ZONE) is a brute-force approach that consists in optimizing  
 296 all reactions rate parameters included in the vector  $\chi^v$  in one step. During this step,  
 297 the whole spatial dimension of the  $N_\phi$  reference premixed flames is targeted:  $\mathcal{A}^P \in$   
 298  $[-\infty, +\infty]$ . Simultaneously the entire range of steady state strained non-premixed  
 299 flamelets is also considered:  $\mathcal{A}^{NP} \in [a_0, a_q]$ . During this step, all kinetic parameters of  
 300 reactions  $R_1^{NO}-R_6^{NO}$  are optimized. As it will be shown further, the too high number of  
 301 kinetic rate parameters optimized in a single step causes the failure of the optimization  
 302 algorithm. A 2-zone optimization method is therefore introduced.

### 303 **3.3. 2-zone optimization (2ZONE)**

304 The optimization procedure is split into two consecutive steps dedicated to the opti-  
 305 mization of fast and slow NO formations process, respectively. To reduce the number of  
 306 free kinetic rate parameters to account at each step, reaction  $R_1^{NO}-R_6^{NO}$  are optimized  
 307 through the two following steps:

- 308 (1) *Flame front block* optimization. Virtual elementary reactions  $R_1^{NO}-R_3^{NO}$  designed  
 309 to capture flame front NO formation are trained to reproduce only fast time  
 310 scales phenomena. Fast time scales learning regions representative of NO forma-  
 311 tion need to be extracted from the whole set of target flames, which gathers here  
 312 premixed and non-premixed flames.
- 313 (2) *Post-flame block* optimization. The virtual elementary reactions  $R_4^{NO}-R_6^{NO}$  are  
 314 optimized to recover the post-flame NO formation which mostly characterize  
 315 premixed flames burnt gases. During the post-flame block optimization, kinetic  
 316 parameters of reactions  $R_1^{NO}-R_3^{NO}$ , issued from the first step, are conserved.  
 317 To ensure consistency between all reactions, the cost function is defined on the  
 318 whole spatial space covered by targeted flamelets, including both flame-front and  
 319 post-flame regions.

320 A criterion is required to distinguish the learning subspaces dedicated to the  
 321 *Flame front* and *Post-flame* optimization steps, respectively. The definition of the  
 322 criterion and the subspaces separation procedure is detailed in Appendix A. For that

323 purpose, two physical quantities ( $\delta_{FF}$  and  $a_{FF}$ ), dedicated respectively to premixed  
 324 and non-premixed flamelets, are defined to distinguish the fast NO formation time  
 325 scale from the slow one.  $\delta_{FF}$  is the critical length scale for premixed flamelets. For  
 326  $x \in [-\infty, \delta_{FF}]$ , fast time scales, characteristics of *prompt* NO, dominate. At the  
 327 opposite *thermal* and *reburning* are more important for  $x \in [\delta_{FF}, +\infty]$ .  $a_{FF}$  is the  
 328 critical strain rate for non-premixed strained flamelets. For  $a \in [a_{FF}, a_q]$  fast NO time  
 329 scales dominate while for  $a \in [0, a_{FF}]$  slow time scales are more important.

330

331 The optimization process is then split into two steps:

332 **Step 1** The *Flame front block* is optimized using flame data characteristic of *prompt*  
 333 NO process. In practice, the cost functions  $C_{NO}^P$  and  $C_{NO}^{NP}$ , computed by Eqs. 20 and  
 334 21, are restricted to the subspaces  $\mathcal{A}^P \in [-\infty, \delta_{FF}]$  and  $\mathcal{A}^{NP} \in [a_{FF}, a_q]$ . During this  
 335 step, only kinetic parameters of reactions  $R_1^{NO}$ - $R_3^{NO}$  are optimized.

336 **Step 2** The *Post-flame block* is optimized using flame data characteristic of *slow*  
 337 NO processes. In practice, the cost functions  $C_{NO}^P$  and  $C_{NO}^{NP}$ , computed by Eqs. 20  
 338 and 21, include the entire premixed flamelet space  $\mathcal{A}^P \in [-\infty, +\infty]$ . Analysis of DNS  
 339 of partial-oxidation processes have shown that, in post-flame regions characterized  
 340 by slow chemistry phenomena, molecular diffusion is less important than chemical  
 341 reaction [43]. According to ILDM theory [28], chemical trajectories followed by  
 342 premixed and non premixed flames in the composition space are therefore identical.  
 343 In the present work, only premixed flamelets are therefore targeted to optimize slow  
 344 NO chemistry:  $\mathcal{A}^{NP} = \emptyset$ . During this step, only kinetic parameters of reactions  
 345  $R_4^{NO}$ - $R_6^{NO}$  are optimized.

346

347 The two learning procedures, 1ZONE and 2ZONE, are now compared on a  
 348 simple test case.

### 349 3.4. Comparison of 1ZONE and 2ZONE optimization procedures

350 The learning database retained to optimize the NO virtual mechanism is made of a  
 351 single stoichiometric CH<sub>4</sub>/air premixed flamelet. Both 1ZONE and 2ZONE optimized  
 352 solutions are *a-posteriori* compared against the targeted solution in Fig. 5. The slow  
 353 NO formation, visible over the entire computational domain, from  $x = 0$  to  $x = 5$  m,  
 354 is fairly well captured by the two algorithms. But the 1ZONE (dashed line) optimized  
 355 scheme fails to capture the prompt NO formation, as evidenced in the inner graph  
 356 which focuses on the thermal flame thickness (from  $x = 0$  to  $x = 25$  mm). This  
 357 inaccuracy is corrected by the 2ZONE (dotted line) algorithm which is able to predict  
 358 both fast and slow NO chemistry.

359 To understand the difference between 1ZONE and 2ZONE, the error  $\epsilon$  between the  
 360 targeted flame data and the two optimized solutions *a-posteriori* obtained with the  
 361 virtual mechanism is introduced:

$$\epsilon(\mathcal{A}') = \frac{\|Y_{NO}^{P,v}(x, \phi^0) - Y_{NO}^{P,d}(x, \phi^0)\|_{L_2}}{\|Y_{NO}^{P,d}(x, \phi^0)\|_{L_2}} \quad \text{for } x \in \mathcal{A}' \quad (22)$$

362 where  $\mathcal{A}'$  is the 1-D spatial subspace on which the error  $\epsilon$  is computed. The three sub-  
 363 spaces  $\mathcal{A}' = [-\infty, +\infty]$ ,  $\mathcal{A}' = [-\infty, \delta_{FF}]$  and  $\mathcal{A}' = [\delta_{FF}, +\infty]$  are retained to measure  
 364  $\epsilon$  along the the *whole flame*, *flame front* region and *post-flame* region, respectively.

365 Figure 6 plots the evolution of these three errors as a function of the generation num-

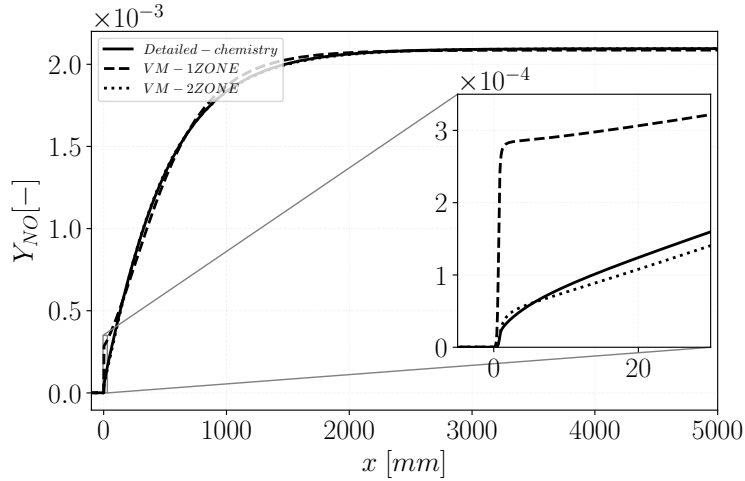


Figure 5.: Comparison of the NO mass fraction computed with virtual chemistry and reference detailed chemistry, at stoichiometric conditions. Virtual chemistry results are shown for the 1-zone optimization (1ZONE) and the 2-zone optimization (2ZONE). The comparison is proposed either over the whole computational domain and in the flame front region.

ber  $N_{gen}$  for both 1ZONE and 2ZONE algorithms.

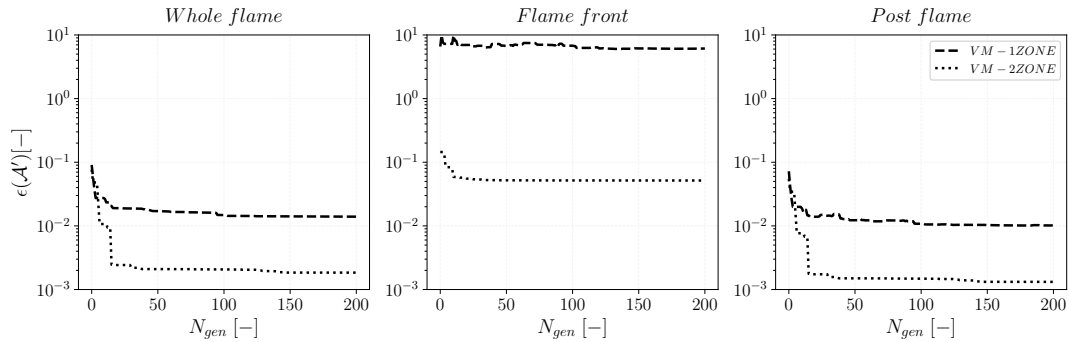


Figure 6.: Error evolution during the optimization procedure.  $N_{gen}$  is the generation number performed by the evolutionary algorithm. The error is shown for the single zone optimization (VM-1ZONE) and for the two zone optimization (VM-2ZONE) and it is computed using three subspaces: *whole flame*, *flame front* and *post-flame* regions.

366

367 The error computed over the *whole domain* decreases as expected with the 1ZONE  
 368 procedure during 15-20 generations and then it reaches a plateau around 2% (Fig.  
 369 6, left). However, better results are observed with the 2ZONE mechanism. With the  
 370 1ZONE procedure, a very poor convergence of the error is observed in the *flame front*,  
 371 which stays above 1000% (Fig. 6, center). The failure of the optimization process is  
 372 supposed to be due to:

373

- the high number of kinetic rate parameters optimized in a single step,
- the wide range of values covered by these parameters to capture both fast and slow NO chemistry pathways.

374

375

376 Results are greatly improved by the 2ZONE algorithm where the convergence of  
 377 the error in the *flame front* is ensured. As a consequence, the error on the prompt  
 378 NO prediction decreases below 5% after 20 generations. In addition, the *post-flame*  
 379 error of the 2ZONE optimization procedure is also decreased by more than an order  
 380 of magnitude compared with the 1ZONE optimization procedure (Fig. 6, right).

#### 381 4. Results: 1-D flames

382 This section presents the 1-D results of the  $R_1^{NO}$ - $R_6^{NO}$  NO virtual mechanism opti-  
 383 mized according to the 2ZONE strategy over CH<sub>4</sub>/air hybrid flamelets. The mecha-  
 384 nism is reported in Appendix. B. Results for premixed freely propagating flames, for  
 385 several mixture equivalence ratios, and for diffusion flames for several flame strain  
 386 rates are presented and compared to simulations carried out with the detailed kinetic  
 387 mechanism.

##### 388 4.1. Virtual mechanism optimization for multi-mode combustion

Figure 7 describes the 2ZONE optimization procedure.

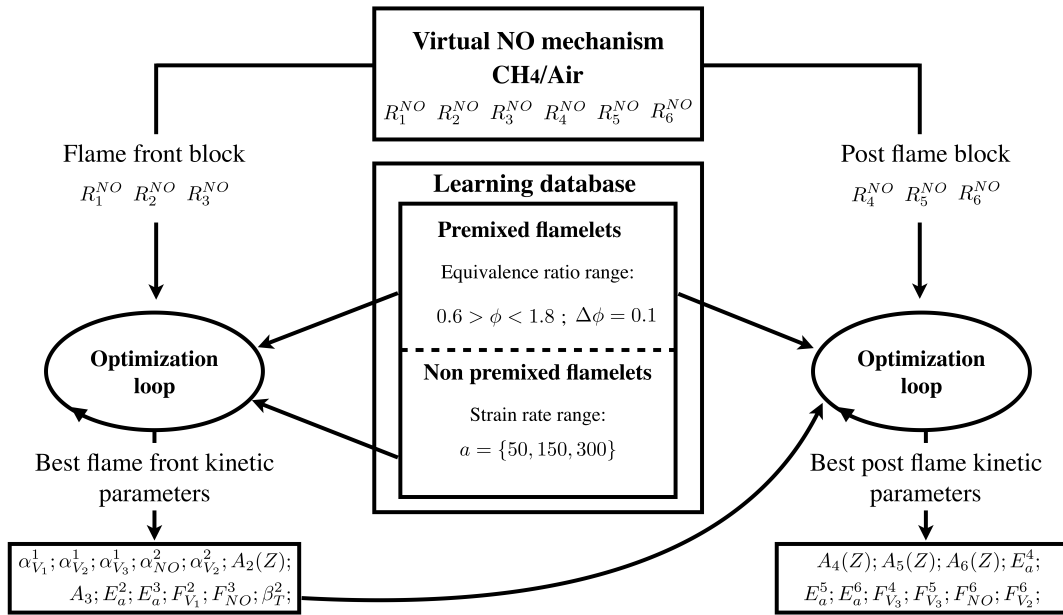


Figure 7.: Virtual NO mechanism optimization procedure applied to CH<sub>4</sub>/air combustion. The 2ZONE optimization is applied.

389 The reference detailed chemistry premixed and non-premixed flamelets are computed  
 390 with the REGATH solver [5] by accounting for differential diffusion and by using  
 391 the GRI3.0 mechanism [3]. The  $N_\phi$  premixed flamelets retained to compute the cost  
 392 function  $C_{NO}^P$  from Eq. 20 cover the whole flammability limit:  $0.6 < \phi_0 < 1.8$ . Varying  
 393 the number of targeted flames  $N_\phi$ , we found an empirical optimal compromise retaining  
 394  $N_\phi = 13$  (or equivalently  $\Delta\phi = 0.1$ ). For 1-D non-premixed counterflow flames, NO  
 395 profiles representative of flames having a strain rate  $a$  greater than the critical value  
 396  $a_{FF} = 50 \text{ s}^{-1}$  are included. As for premixed flames, an empirical optimal solution was  
 397



398 found for the strain-rate discretization  $\Delta a$  so as to ensure a compromise between the  
 399 convergence of the optimization algorithm and the precision of the mechanism over the  
 400 whole range of strain rates. For this application, the subspace  $\mathcal{A}^{NP} = \{50, 150, 300\}$   
 401  $\text{s}^{-1}$  is retained to build up the non-premixed learning library.

402

403 Three virtual mechanisms of different sizes are generated in order to assess the influence  
 404 of the number of virtual species / reactions. The complete virtual mechanism  $R_1^{NO}$ -  
 405  $R_6^{NO}$  is indicated with the abbreviation VM-6R. Two smaller mechanisms VM-4R and  
 406 VM-5R are also considered. VM-4R is obtained by removing  $R_4^{NO}$  and  $R_5^{NO}$  from the  
 407 VM-6R mechanism. Whereas three reactions  $R_1^{NO}$ - $R_3^{NO}$  are dedicated to capture fast  
 408 processes, only  $R_6^{NO}$  is kept to handle slow time scales and to retrieve equilibrium  
 409 conditions. At the opposite VM-5R is designed by removing  $R_3^{NO}$  from the VM-6R  
 410 mechanism. The three elementary reactions  $R_4^{NO}$ - $R_6^{NO}$  are retained for slow process,  
 411 while the number of "fast" elementary reactions is restricted to  $R_1^{NO}$  and  $R_2^{NO}$ . Table  
 1 summarizes the three mechanism's properties.

Table 1.: Summary of the three optimized virtual NO mechanisms. The virtual reac-  
 tions that are included in each mechanism are indicated.

Mechanisms	Reactions	Reaction nb. for <i>Flame front</i>	Reactions nb. for <i>Post flame</i>	Species nb.
VM-6R	$R_1^{NO}$ - $R_6^{NO}$	3	3	6
VM-4R	$R_1^{NO}$ - $R_3^{NO}$ $R_6^{NO}$	3	1	5
VM-5R	$R_1^{NO}$ - $R_2^{NO}$ $R_4^{NO}$ - $R_6^{NO}$	2	3	6

412

413 Molecular diffusive fluxes of species belonging to both main and NO virtual schemes  
 414 are modeled with a unity Lewis number assumption. However, as discussed in [1], this  
 415 assumption still enable a correct prediction of unstretched laminar flame consumption  
 416 speed and species profiles across planar flame fronts, as the targeted 1-D flame solutions  
 417 used to calibrate the main virtual scheme include differential diffusion effects.

#### 418 4.2. Premixed flames

419 VM-6R results are *a-posteriori* compared versus the reference detailed chemistry so-  
 420 lutions, for three different equivalence ratios: lean ( $\phi = 0.6$ ), stoichiometric ( $\phi = 1.0$ )  
 421 and rich ( $\phi = 1.6$ ). The results are presented in the flame front and in the post-flame  
 422 regions in Fig.8. The proposed 6-reaction mechanism allows to correctly reproduce  
 423 prompt and thermal post-flame NO formation characterizing lean and stoichiomet-  
 424 ric conditions. The post-flame NO re-burning phenomena, encountered in rich flame  
 425 conditions, are also correctly described.

426 A comparison is now proposed to stress the role of reactions  $R_4^{NO}$  and  $R_5^{NO}$  in the  
 427 mechanism. Figure 9 compares, for a rich ( $\phi = 1.6$ ) and a stoichiometric flames, the  
 428 results obtained with the two mechanisms VM-4R and VM-6R against the detailed  
 429 chemistry solutions. It shows that the two reactions  $R_4^{NO}$  and  $R_5^{NO}$  are required to cap-  
 430 ture the slow NO reburning already illustrated in Fig. 1. These reactions are however  
 431 not necessary for lean, stoichiometric and moderately rich conditions ( $\phi < 1.4$ ), where  
 432 reburning phenomena is not significant. Consequently VM-4R and VM-6R solutions

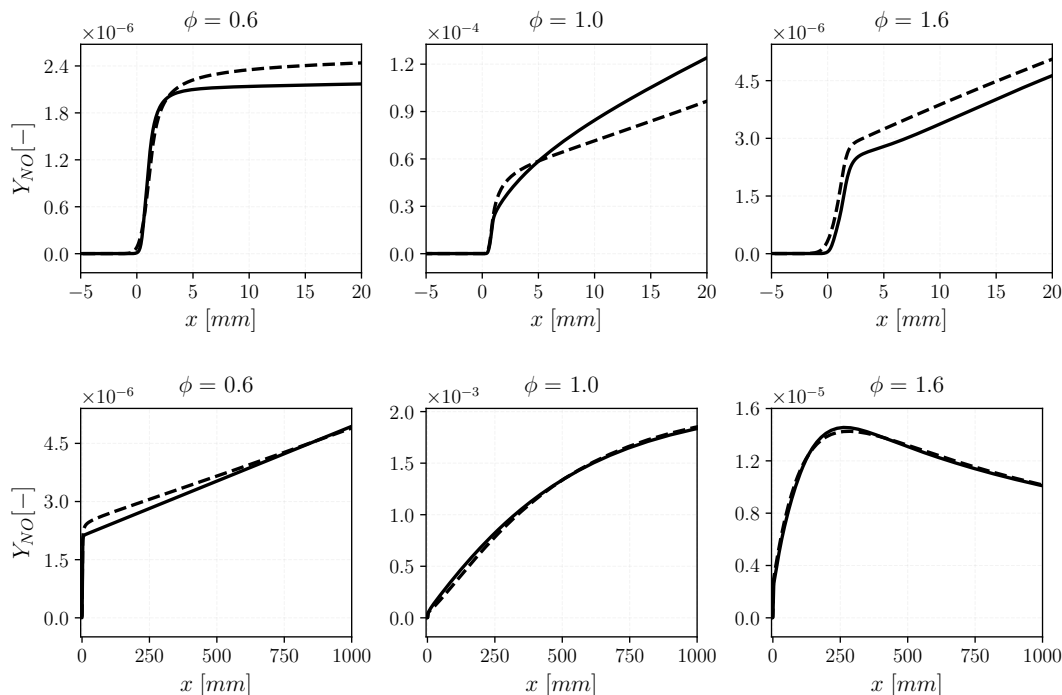


Figure 8.: NO mass fraction profiles for a lean ( $\phi = 0.6$ ), a stoichiometric ( $\phi = 1.0$ ) and a rich ( $\phi = 1.6$ ) equivalence ratio. Virtual chemistry VM-6R NO (dashed lines) is compared versus the reference detailed chemistry (solid lines). Results are presented at the flame front (upper figures) and post-flame (lower figures) spatial scales.

433 collapse on the same curve for  $\phi < 1.4$  as illustrated in Fig. 9 (right).

#### 434 4.3. Non-premixed flames

435 1-D non-premixed counterflow flames are *a-posteriori* computed with the entire opti-  
 436 mized virtual mechanism VM-6R. Figure 10 shows the NO profile computed with the  
 437 whole virtual NO mechanism VM-6R, and the reference profiles, for two different flame  
 438 strain rates. The proposed virtual NO mechanism optimized to fit both premixed and  
 439 non-premixed flame archetypes retrieves the high sensitivity of the NO profile to the  
 440 flame strain rate. Decreasing the flame strain rate, the residence time increases and  
 441 consequently the NO formation is higher. However, virtual NO mechanism VM-6R  
 442 does not perfectly describe the fast NO mass fraction decay on the flame rich side,  
 443 which characterizes detailed chemistry profiles. It turns out difficult to find a better  
 444 compromise between premixed and non-premixed flames in the flame front region with  
 445 only two reactions ( $R_2^{NO}$ - $R_3^{NO}$ ).

446 Comparison between VM-6R and VM-5R, in which reaction  $R_3^{NO}$  has been removed  
 447 before the optimization process, is also shown in Fig. 10. The large discrepancy ob-  
 448 served between VM-5R and the detailed chemistry solutions confirms that  $R_3^{NO}$   
 449 is required in the flame front block to capture NO formation in non-premixed flames.  
 450 Without it, the virtual mechanism does not have enough degrees of freedom to capture  
 451 NO formation in both premixed and non-premixed flame regimes.

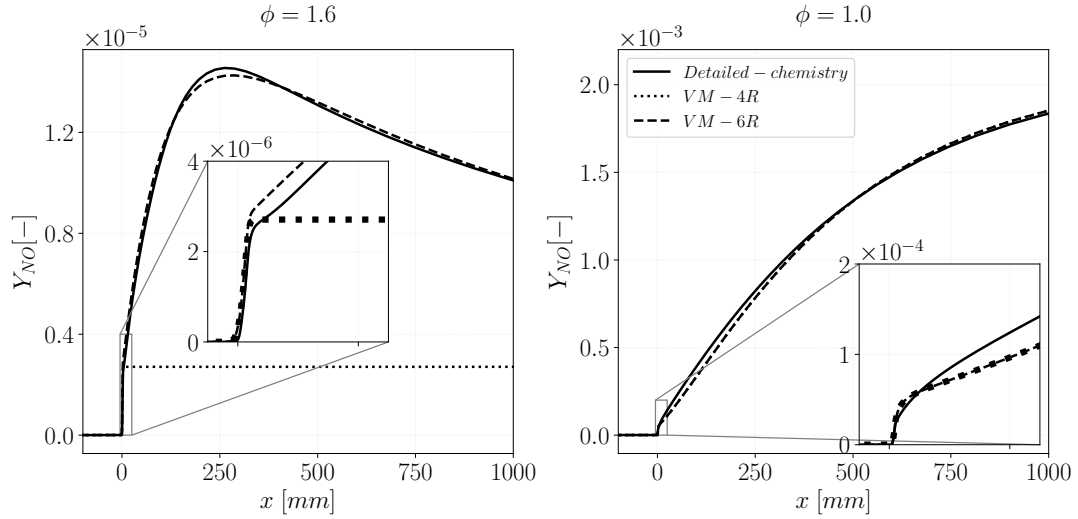


Figure 9.: Comparison of NO mass fraction from detailed chemistry and virtual chemistry for a rich (left) and a stoichiometric (right) 1-D premixed flames. Two virtual mechanism are shown: the first retains 1 reaction only in the post-flame block (VM-4R) and the second retains the whole post-flame block (VM-6R).

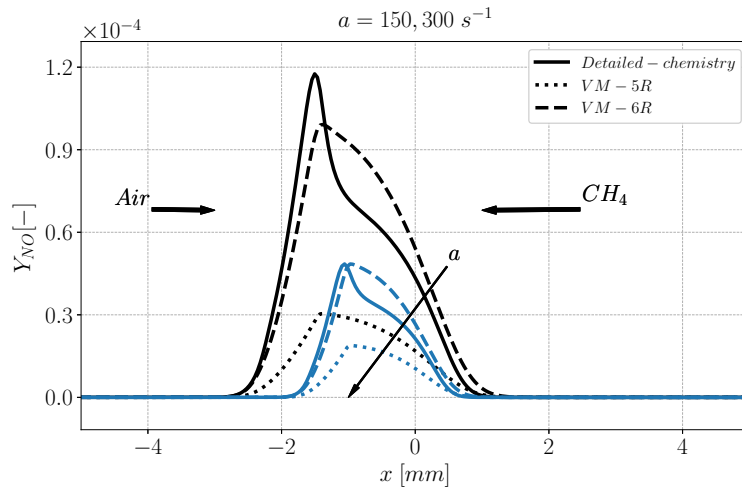


Figure 10.: NO mass fraction profiles in non-premixed counterflow flames for two strain rate values ( $150$  and  $300 \text{ s}^{-1}$ ). Detailed chemistry and virtual chemistry results are compared. Two virtual mechanisms are shown: the first considers 2 reactions only in the flame front block (VM-5R) and the second considers the whole flame front block (VM-6R). Different colors are used for different strain rates.

## 452 5. 2-D slots burner flames

453 In the current section, virtual chemistry is challenged in 2-D CFD computations and  
 454 compared against detailed chemistry simulations. The simulations are carried out for  
 455 several 2-D laminar flame benchmarks including a premixed, a non-premixed and a  
 456 partially premixed flame.

457 The CFD code laminarSMOKE [42] is used to perform the computations for both  
 458 detailed chemistry and virtual chemistry. The laminarSMOKE code is based on the  
 459 open-source suite OpenFOAM [44]. It has already shown capability to accurately  
 460 model laminar flames including detailed chemistry using hundreds of species and re-  
 461 actions [45, 46]. The transport equations of mass, momentum, energy, and species are  
 462 solved based on the operator-splitting approach [47].

### 463 5.1. Premixed flame

464 The premixed single slot burner geometry consists of a 2-D rectangular computational  
 465 domain whose dimensions are shown in Fig. 11. The boundary conditions include an  
 466 inlet, an outlet and adiabatic walls. Since the configuration is axial-symmetric only a  
 467 half of the computational domain is simulated. The other half of the computational  
 468 domain is obtained by symmetric reflection of the first part. Therefore a symmetry  
 boundary condition is imposed along the axis.

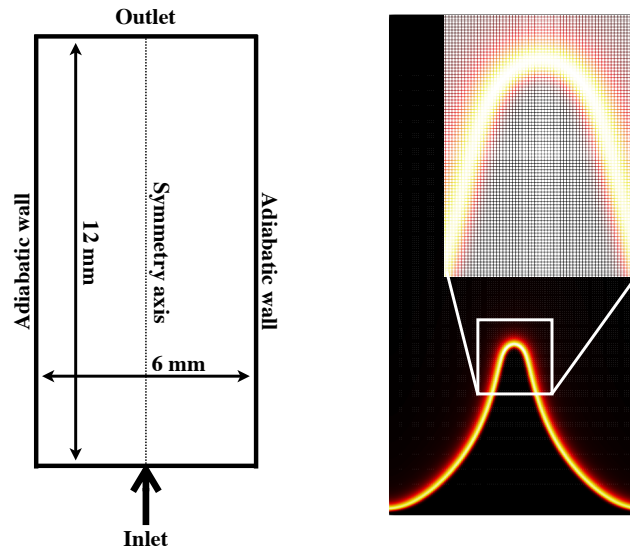


Figure 11.: 2-D premixed slot burner numerical set-up. On the left schematic view of the computational domain with the corresponding dimensions and the boundary conditions. On the right the normalized heat release rate from numerical simulation shown on the computational grid.

469 At the inlet, a developed laminar parabolic velocity profile is prescribed in the  
 470 axial direction using a mean value  $U_m = 0.6 \text{ m/s}$ , whereas the others velocity  
 471 components are set equal to zero. A cartesian grid is considered in the simulation.  
 472 The characteristic cell size is of about  $\sim 0.015 \text{ mm}$ . This cell size allows to fully  
 473 resolve the thermal flame thickness and the heat release rate of a premixed laminar  
 474 flame. In particular, the employed mesh size ensures 15 to 20 cells across the thermal  
 475 flame thickness. A zoom on the computational grid, in the flame tip region, is made  
 476 in Fig. 11 and an example of normalized heat release rate is also shown on the com-  
 477 putational grid. Indeed the heat release rate is properly solved over the employed grid.

478 Figure 12 shows the temperature and NO field for the 2-D premixed burner at  
 479

481 three different equivalence ratios (0.8, 1.0 and 1.2). Virtual chemistry results are  
482 directly compared to detailed chemistry ones. The temperature field predicted by the  
483 main virtual mechanism is in good agreement with the detailed chemistry, for the  
484 three equivalence ratios. It is remarkable that the flame height is properly captured  
485 by virtual chemistry. At  $\phi = 1.2$  a misprediction by about 10% is however observed,  
486 which is attributed to species transport phenomena. As discussed in [1], as long as  
487 1-D detailed chemistry flamelets computed under differential diffusion assumptions  
488 are targeted, differential diffusion phenomena in the direction normal to the flame  
489 front are well captured, even if unity Lewis number assumption is made to close the  
490 virtual species balance equations. In 2-D and 3-D, molecular diffusions effects are  
491 however not correctly tackled, causing a difference in the flame curvature description  
492 and on the flame height, especially visible under rich conditions.

493 The virtual NO field agrees well with the temperature field: when temperature  
494 increases earlier for virtual chemistry (as for  $\phi = 1.2$ ), NO increases earlier too. The  
495 2-D slot burner configuration, retained in the present work allows to observe mostly  
496 the whole prompt NO formation and the first part of the thermal one. However, as  
497 observed in the 1-D premixed profiles in Fig. 9, NO is further produced in the burnt  
498 gases, for longer residence time, through the thermal route. An underestimation of  
499 the NO level is observed at  $\phi = 0.8$  and 1.0, whereas a better prediction is observed  
500 for  $\phi = 1.2$ . This behavior is in accordance with the 1-D profiles shown in Fig. 8 at  
501 the flame front scale.

502  
503 For the stoichiometric slot burner flame, 1-D temperature and NO mass frac-  
504 tion profiles are extracted from the 2-D field over both axial and a radial directions.  
505 The 1-D sections, used for the comparison, are indicated by white lines in Fig. 12.  
506 Figure 13 shows the temperature and NO profiles from virtual and from detailed  
507 chemistry computations along the two lines in the axial direction ( $x=0$  mm) and for a  
508 radial section ( $y= 2$  mm). The temperature agreement in the axial direction confirms  
509 that the flame height is well retrieved even if a slight shifting in the radial direction  
510 is observed. This discrepancy might be due to the non-perfect reproduction of flame  
511 curvature effects.

## 512 **5.2. Non-premixed flame**

513 A 2-D non-premixed laminar coflow flame is simulated in the present section. The  
514 considered configuration along with the main burner dimensions and the boundary  
515 conditions set-up are schematized in Fig. 14. The figure also shows a normalized heat  
516 release rate field over half of the computational domain region close to the burner  
517 nozzle. A fuel jet is surrounded by a pure air coflow allowing the development of a  
518 non-premixed diffusion flame. The computational geometry is symmetric with respect  
519 to the centreline axis, as for the premixed single slot burner; consequently, just a half  
520 of the computational domain is computed. Adiabatic walls are imposed close to the air  
521 inlet whereas an inlet/outlet boundary condition [44] is prescribed on the burner side.

522  
523 A 2-D non uniform structured rectangular mesh is used in the simulations as  
524 proposed by Cuoci *et al.* [42, 45]. The characteristic mesh size in the flame front  
525 region is of about  $\sim 0.05$  mm which is sufficient to ensure a proper flame resolution  
526 in diffusion flame conditions. Velocity boundary conditions are tuned to ensure the  
527 flame attachment to the burner lip avoiding any flame lift-off. Flat velocity profiles

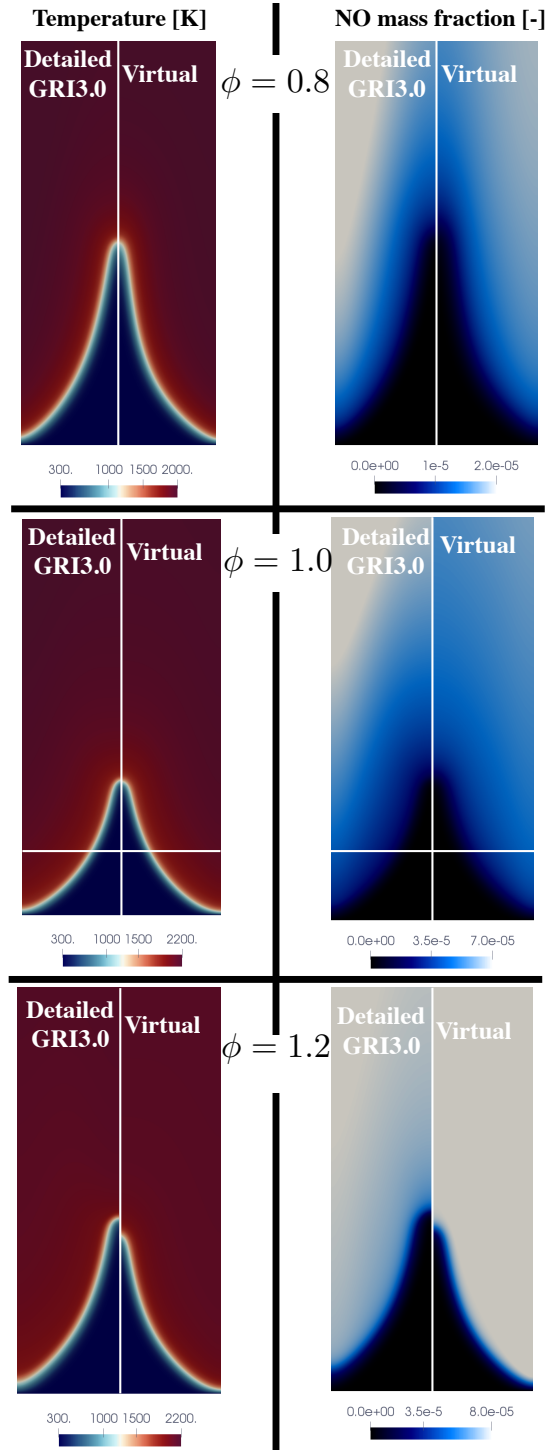


Figure 12.: Temperature and NO mass fraction colormaps for the 2-D laminar single slot burner (Bunsen flame). Virtual chemistry solution is compared with detailed chemistry one.

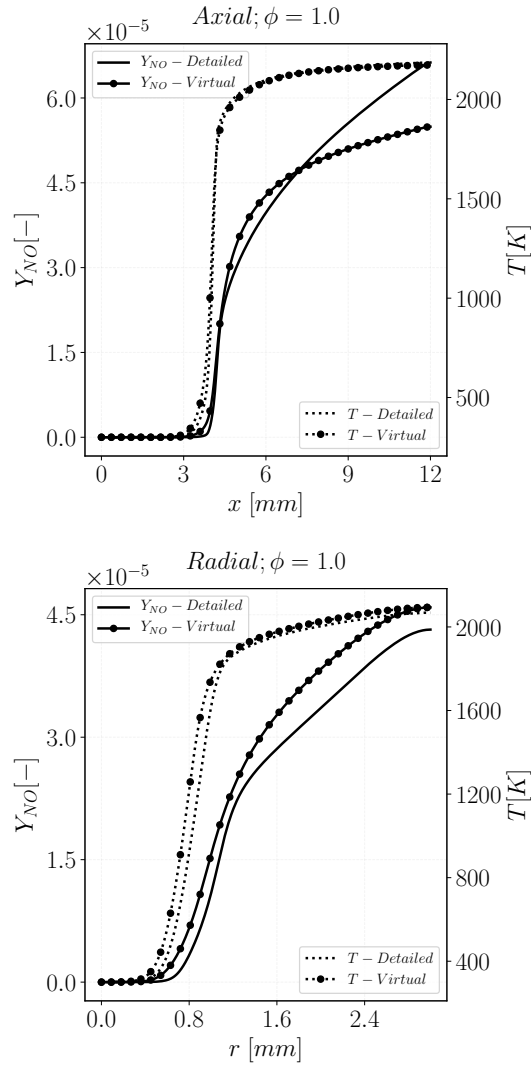


Figure 13.: Virtual chemistry (symbols + lines) is compared against detailed chemistry (lines) for temperature (dashed lines) and NO mass fraction (solid lines). Top: axial profiles. Bottom: radial profiles at the centerline distance  $x = 2$  mm.

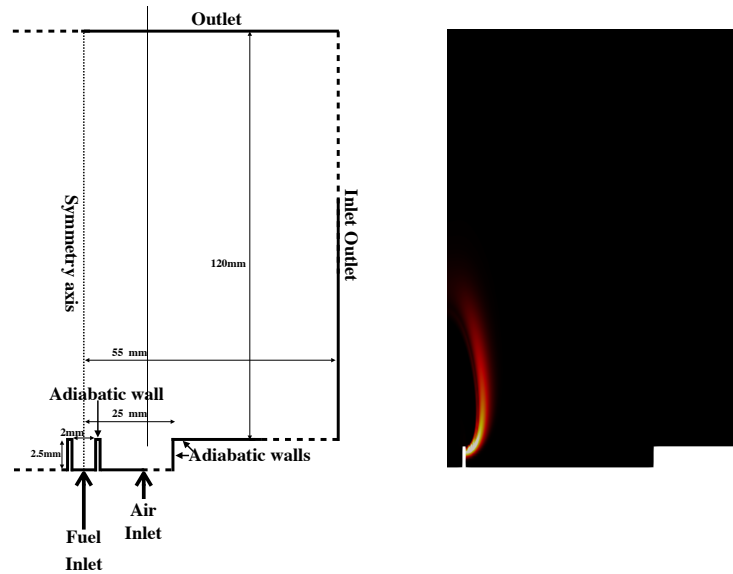


Figure 14.: Numerical set-up of the coflow diffusion flame burner. On the left a schematic view of the 2-D simulated domain is presented. The main burner dimensions and the prescribed boundary conditions type are shown. On the right an example of normalized heat release rate computed from detailed chemistry simulation is shown.

528 at 0.15 m/s are prescribed in the two streams. Pure  $CH_4$  and pure air at 300 K are  
 529 injected in the *Fuel Inlet* and the *Air Inlet*, respectively.

530

531 Figure 15 shows the temperature and NO mass fraction fields for the 2-D dif-  
 532 fusion flame configuration, comparing virtual chemistry to the detailed chemistry  
 533 results. The virtual chemistry flame shape is close to the detailed chemistry one,  
 534 but it appears more compact. In the virtual chemistry simulation, temperature  
 535 increases faster than with detailed chemistry. The NO mass fraction field predicted  
 536 by virtual chemistry is correctly located in the computational domain with respect to  
 537 temperature field.

538

539 Figure 16 compares the temperature and NO mass fraction along the flame  
 540 axis. As virtual chemistry temperature rises faster, NO mass fraction presents an  
 541 early peak at  $x = 0$  mm. Successively the small NO reburning corresponding to  
 542 detailed chemistry is overestimated by virtual chemistry. This reburning phenomenon  
 543 in coflow flame configuration has been already observed by Cuoci *et al* [42]. The max  
 544 NO peak prediction, corresponding to the temperature peak is correctly predicted.  
 545 However, the amplitude of NO mass fraction is relatively overestimated. This phe-  
 546 nomenon is attributed to the slight temperature overestimation. After the peak zone,  
 547 the NO reduction due to consumption and/or dilution effects is correctly captured.

### 548 **5.3. Partially-premixed flame**

549 The developed NO virtual mechanism is finally assessed in a partially premixed  
 550 flame configuration. The considered geometry and mesh are the same as the diffusion  
 551 flame configuration, described in the previous section. In the central jet (*Fuel Inlet*)



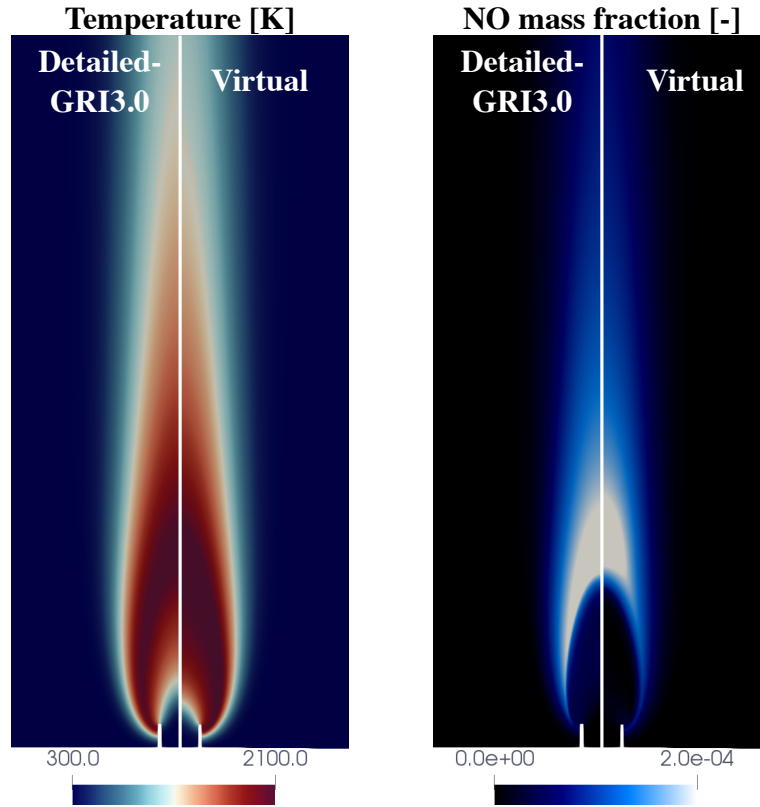


Figure 15.: Temperature and NO mass fraction fields from numerical simulations for the diffusion flame. The virtual chemistry results are compared versus the reference GRI3.0 solutions.

552 a premixed mixture of fuel and air, above the flammability limit, is injected. An  
 553 equivalence ratio equal to 2.5 and a temperature of 300K are prescribed. Pure ambient  
 554 air at 300K, as for the diffusion flame configuration, is injected through the *Air Inlet*  
 555 tube. Inlet velocities are tuned to stabilize the flame at the burner lips, without  
 556 having any lift-off. A flat velocity profiles of 0.35 *m/s* and 0.05 *m/s* are prescribed at  
 557 the *Fuel Inlet* and the *Air Inlet*, respectively.

558

559 Figure 17 shows the temperature and NO mass fraction 2-D fields for the partially  
 560 premixed flame. The flame is stabilized at the same position with detailed and  
 561 virtual chemistry. NO field is correctly located over the computational domain, but  
 562 the NO peak value is overestimated.

563 Figure 18 shows the temperature and NO profiles along the axis. The NO 1-D profile  
 564 confirms the correct prediction of the NO peak position but its value is overestimated.

565

#### 566 **5.4. CPU cost comparison**

567 A comparison to evaluate the CPU ratio between detailed chemistry and virtual chem-  
 568 istry simulation was carried out. The stoichiometric 2-D premixed slot burner is com-  
 569 puted for the same physical time (10 ms), using the same numerical set-up and em-

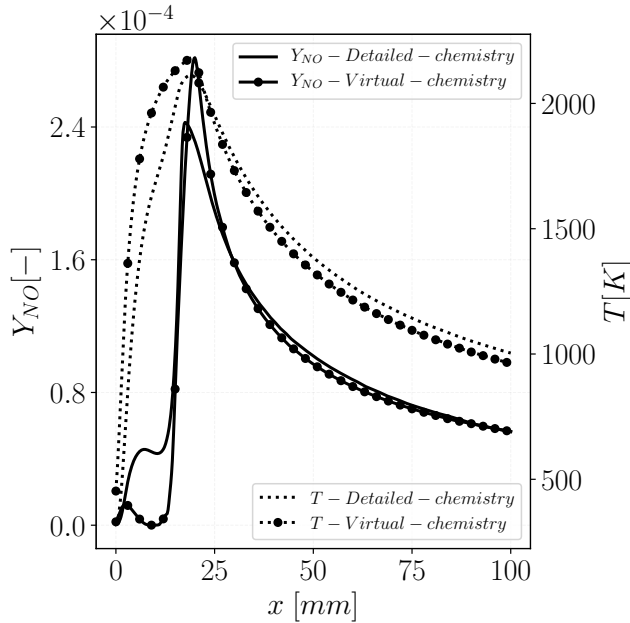


Figure 16.: Temperature (dashed lines) and NO mass fraction (solid lines) along the centerline axis of the 2-D coflow non-premixed flame. Virtual chemistry (symbols + lines) is compared against detailed chemistry (lines).

ploying the same numbers of processors for virtual and detailed chemistry.

Table 2.: CPU cost comparison between detailed reference chemistry and virtual chemistry computations. Main temperature mechanism and the NO one are considered for virtual chemistry.

Mechanism	Nb. species	$C = t^d/t^v$
GRI3.0 [3]	53	39
Virtual Mech.	12	1

570

571 Table 2 summarizes the results of the comparison. The CPU time ratio  $C = t^d/t^v$  that  
 572 compares the detailed ( $t^d$ ) and virtual chemistry ( $t^v$ ) computational time, is equal  
 573 to = 39. The drastic CPU cost reduction is mainly due to the species and reactions  
 574 reduction. The observed CPU speed-up is equal to:

$$C = \frac{t^d}{t^v} \simeq \left( \frac{n^d}{n^v} \right)^{2.5} \quad (23)$$

575 where  $n^d$  (=53) and  $n^v$ (=12) are respectively the number of species included in the  
 576 detailed and virtual mechanisms. This result is in accordance with previous numerical  
 577 studies that use implicit solvers. [48, 49]. This CPU result analysis is valid for any  
 578 2-dimensional laminar computation (premixed, non-premixed and partially premixed)  
 579 performed with laminarSMOKE solver [42].

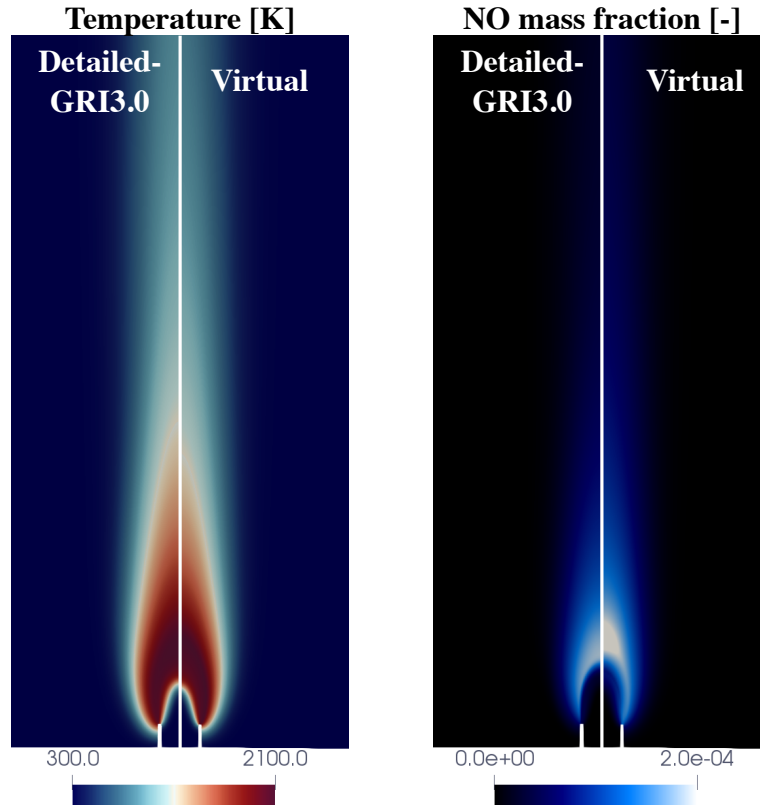


Figure 17.: Temperature and NO mass fraction fields from numerical simulations for the partially-premixed flame. The virtual chemistry results are compared versus the reference GRI3.0 solutions.

## 580 6. Conclusions

581 The virtual chemistry strategy has been retained to develop a new pollutant reduced  
 582 mechanism devoted to NO prediction. The original virtual chemistry formulation has  
 583 been used to predict flame temperature and heat release rate. An NO virtual mecha-  
 584 nism has been designed using a reduced set of virtual species and reactions and trained  
 585 over a hybrid flamelet database, made of premixed and non-premixed 1-D flames.

586 A two-step optimization strategy has been developed to separate and to indepen-  
 587 dently optimize the virtual reactions dedicated to flame front and post-flame NO  
 588 chemistry, respectively. The proposed model is able to describe all the NO chemistry  
 589 pathways exhibited by the reference flame solution. In particular *prompt* NO, *ther-*  
 590 *mal* NO and post-flame NO *reburning* are correctly described by the virtual chemistry  
 591 model. The developed NO virtual mechanism has been tested in 2-D laminar premixed,  
 592 non-premixed and partially premixed flame computations. A comparison to detailed  
 593 reference chemistry has also been proposed. In the CFD computations, the final CPU  
 594 cost associated with the virtual chemistry simulation is drastically smaller than with  
 595 the detailed chemistry one (of about 40 times).

596 The thermodynamics and kinetics parameter are automatically optimized but the  
 597 design of the virtual chemistry architecture remains based on a physically-based ap-  
 598 proach. Despite the promising application to NO chemistry, the empirical identification  
 599 of the optimal number of virtual species and reactions network may become problem-

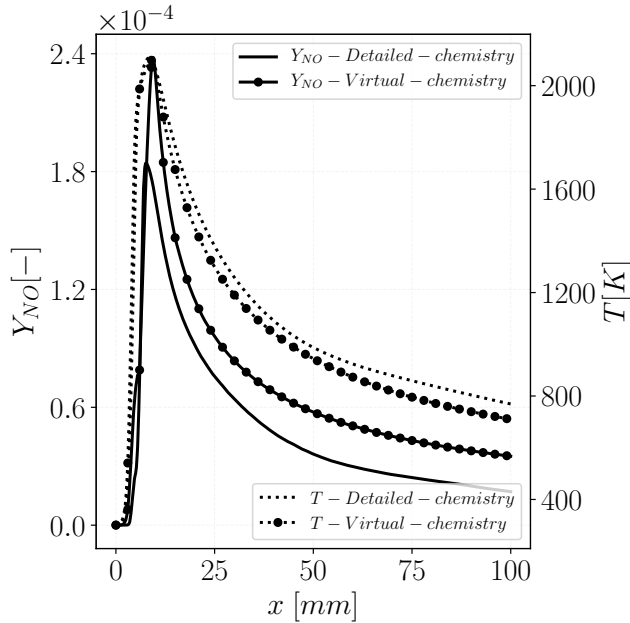


Figure 18.: Temperature (dashed lines) and NO mass fraction (solid lines) along the centerline axis of the 2-D coflow partially premixed flame. Virtual chemistry (symbols + lines) is compared against detailed chemistry (lines).

600 atic in more complex systems where relevant chemical time scales and trajectories are  
 601 more numerous. To overcome this current limitation, automatic methods to build-up  
 602 of the virtual chemistry network, from a time scale analysis of the detailed chemical  
 603 scheme, are under investigation.

## 604 7. Acknowledgements

605 The authors warmly acknowledge Prof. Nasser Darabiha for the useful discussions  
 606 about the model and the numerical simulations. This project has received funding  
 607 from the European Union's Horizon 2020 research and innovation programme under  
 608 the Marie Skłodowska-Curie grant agreement No 643134. This work was granted access  
 609 to the HPC resources under the allocations A0032B10253 made available by GENCI  
 610 (Grand Equipement National de Calcul Intensif).

## 611 Appendix A. NO optimization criterion: zone separation and learning 612 database definition

613 The objective is to find a criterion to dissociate learning subspaces characteristic of fast  
 614 (prompt) and slow (thermal and reburning) NO chemistry in both premixed and non-  
 615 premixed flame archetypes. For premixed flames a spatial length scale  $\delta_{FF}$  is defined  
 616 to separate the computational domain in a *flame front* region and a *post-flame* one.  
 617 A corresponding mixing time scale  $a_{FF}$  is identified for non-premixed flames.

618 **A.1. Criterion definition**

619 In the premixed flamelet database, for each fresh gas equivalence ratio  $\phi^0$ , targeted  
 620 thermo-chemical variables  $\varphi$  such as the temperature and the species mass fractions  
 621 are expressed in terms of the spatial coordinate  $x$ , that correspond to the direction  
 622 normal to the flame front.  $\varphi$  therefore reads:

$$\varphi = \varphi_p(\phi^0, x_p) \quad (\text{A1})$$

623 where  $p$  subscript denotes solutions of premixed flame configurations.

624 Examples of NO mass fractions profiles are plotted in Fig. A1 for three different  
 625 fresh gas equivalence ratio values (the corresponding mixture fraction value is also  
 626 indicated in the figure). The transition between fast NO (in the flame front) and slow  
 627 NO (in the post-flame) kinetics affects the second order material derivative of NO  
 628 mass fraction, related to the second order derivative of  $Y_{NO}$  in steady state, as follows:

$$\frac{D^2 Y_{NO}}{Dt^2} = u^2 \frac{d^2 Y_{NO}}{dx_p^2} = \gamma(x_p) \quad (\text{A2})$$

629 where  $u$  is the flow velocity. The dimensionless  $\gamma$  and the dimensionless  $Y_{NO}$  second  
 630 derivative are defined as follows:

$$\gamma^+ = \frac{|\gamma(x_p)|}{\max |\gamma(x_p)|}; \quad \eta^+ = \frac{\left| \frac{d^2 Y_{NO}(x_p)}{dx_p^2} \right|}{\max \left( \left| \frac{d^2 Y_{NO}}{dx_p^2} \right| \right)} \quad (\text{A3})$$

631 Figure A1 also plots  $\gamma^+$  and  $\eta^+$  in the three premixed CH<sub>4</sub>/air flames previously  
 632 introduced. The transition between flame front and post-flame NO formation is iden-  
 633 tified using the dimensionless absolute value of the second derivative  $\eta^+$ .

634 When  $\eta^+$  becomes lower than a certain threshold on the post-flame side the transi-  
 635 tion between fast and slow NO formation phenomena is defined at the spatial location  
 636  $x_p$  which satisfy the following condition:

$$\eta^+ = \varepsilon \quad (\text{A4})$$

637 where  $\varepsilon$  is a user-defined threshold value. Equation A4 admits an ensemble of solutions  
 638  $\{x_1^p, \dots, x_n^p\}$ . Among this ensemble of solutions, the flame front NO reaction layer  $\delta_{FF}$   
 639 is defined so that fast NO chemistry is completed within the interval  $[-\infty, \delta_{FF}]$ :

$$\delta_{FF}(\phi^0) = \max\{x_{p1}, \dots, x_{pn}\} \quad (\text{A5})$$

640 where  $x_p = 0$  represents the beginning of the flame, defined here as the location  
 641 where the flame temperature  $T$  rises  $10K$  with respect to the fresh gases temperature  
 642  $T^{fg}$ . For premixed flame configurations, the *flame front* region and the *post-flame* one  
 643 corresponds to the 1-D domains  $\mathcal{A}^P \in [-\infty, \delta_{FF}]$  and  $\mathcal{A}^P \in [\delta_{FF}, \infty, ]$ , respectively.

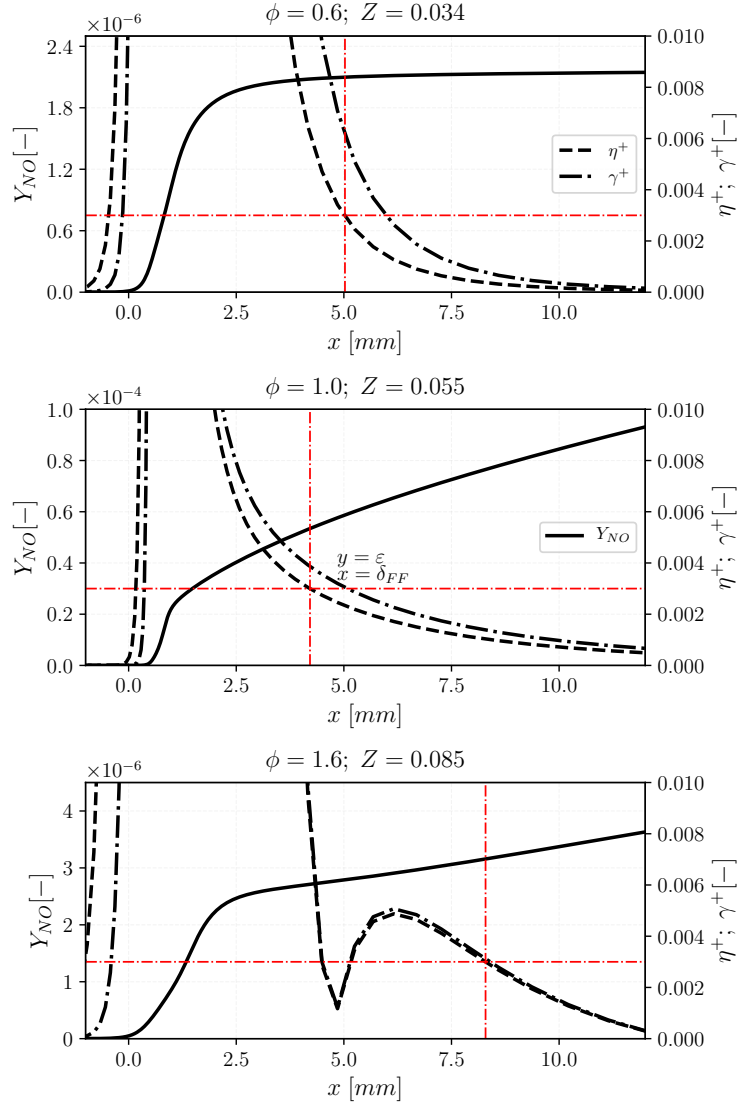


Figure A1.: NO mass fraction and the dimensionless  $\eta^+$  and  $\gamma^+$  quantities from detailed chemistry computations for different equivalence ratio values. The corresponding mixture fraction  $Z$  is also indicated for each flame.

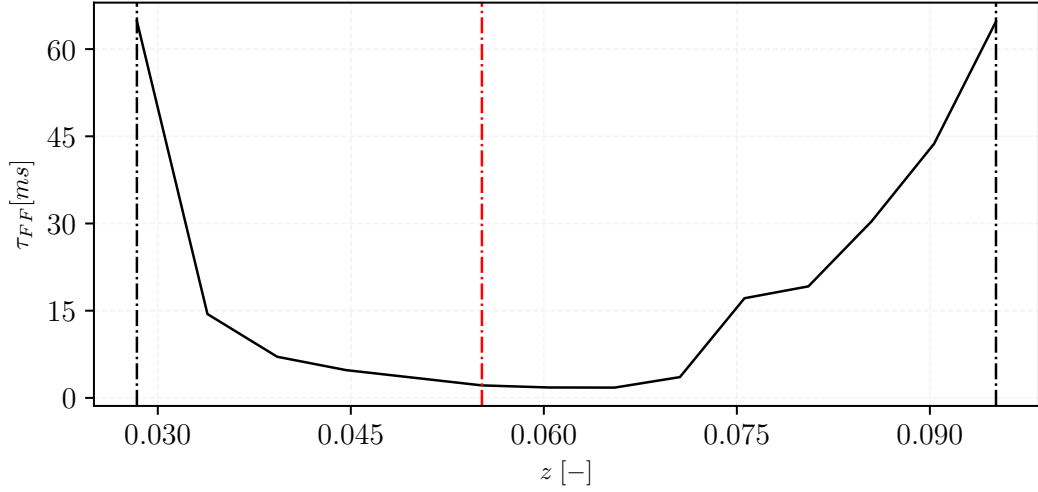


Figure A2.: Flame front residence time as function of mixture fraction. The stoichiometric mixture fraction, lean and rich flammability limits are also shown through the three vertical lines.

644 A cut-off time scale  $\tau_{FF}$  between fast and slow NO chemistry is also introduced  
 645 as the Lagrangian residence time taken by the fresh gases to reach  $\delta_{FF}$  in premixed  
 646 flames.  $\tau_{FF}$  is defined as follows:

$$\tau_{FF}(\phi^0) = \int_0^{\delta_{FF}(\phi^0)} \frac{1}{u_p(\phi^0)} dx, \quad (\text{A6})$$

647 A mixture fraction  $Z$  is uniquely defined from the fresh gases equivalence ratio  $\phi^0$   
 648 to reach 0 in pure air and 1 in pure fuel.  $\tau_{FF}$  is plotted in Fig. A2 as function of the  
 649 mixture fraction  $Z$  in the whole flammability limit. The cut-off time scale averaged  
 650 over the whole flammability domain reads:

$$\bar{\tau}_{FF} = \frac{1}{(Z^r - Z^l)} \int_{Z^l}^{Z^r} \tau_{FF}(Z) dZ, \quad (\text{A7})$$

651 where  $Z^l$  and  $Z^r$  are values of mixture fraction at the lean and rich flammability limits,  
 652 respectively.

### 653 **A.2. Extension to non-premixed counterflow flames**

654 To identify the non-premixed flames that have to be included in the flame front op-  
 655 timization database, the averaged cut-off time scale  $\bar{\tau}_{FF}$ , previously defined, is used.  
 656 It is assumed that the transition time scale between fast and slow NO chemistry is of  
 657 the same order of magnitude for premixed and non-premixed flames. As consequence,  
 658  $\bar{\tau}_{FF}$  is here employed to estimate the critical strain rate, characteristic of non-premixed  
 659 counterflow flames using the following simplified relation:

Table B1.: Virtual NO sub-mechanisms kinetic rate parameters. Units are: cm, s, cal, mol and K

Reaction	$A_i^{NO}$	$E_a^{NO,i}$	$\beta_T^{NO,i}$	$F_k^{NO,i}$	$\alpha_k^{NO,i}$
$R_1^{NO}$	$1.5 \times 10^{18}$	$3.5 \times 10^4$	-		$\alpha_{V_1}^{NO,1} = 0.14$
				$F_F^{NO,1} = 1.71$	$\alpha_{V_2}^{NO,1} = 0.76$
				$F_{Ox}^{NO,1} = 0.87$	$\alpha_{V_3}^{NO,1} = 0.10$
$R_2^{NO}$	$1.9 \times 10^{24}$	$7.6 \times 10^4$	-0.08	$F_{V_1}^{NO,2} = 1.24$	$\alpha_{NO}^{NO,2} = 0.020$ $\alpha_{V_2}^{NO,2} = 0.98$
$R_3^{NO}$	$1.1 \times 10^{18}$	$4.7 \times 10^3$	-	$F_{NO}^{NO,3} = 3.34$	-
$R_4^{NO}$	$5.5 \times 10^{25}$	$2.4 \times 10^5$	-	$F_{V_3}^{NO,4} = 1.07$	-
$R_5^{NO}$	$4.4 \times 10^{17}$	$1.2 \times 10^5$	-	$F_{V_3}^{NO,5} = 1.76$	-
$R_6^{NO}$	$3.6 \times 10^{21}$	$2.2 \times 10^5$	-	$F_{NO}^{NO,6} = 0.19$	
				$F_{V_2}^{NO,6} = 0.97$	-

$$a_{FF} = 1/\bar{\tau}_{FF}. \quad (\text{A8})$$

660 All flamelets computed with a strain rate higher than  $a_{FF}$  ( $\mathcal{A}^{NP} \in [a_{FF}, a_q]$ ) will  
661 serve as a target for optimizing the *flame front* chemistry block (reactions  $R_1^{NO}$ - $R_3^{NO}$ ).

## 662 Appendix B. NO sub-mechanism for CH<sub>4</sub>/Air

663 Table B1 gives the optimized kinetic rate parameters for the NO-virtual sub-  
664 mechanism: For pre-exponential constants that are mixture-fraction dependent the  
665 value is reported at stoichiometry.

666 The correction functions  $f_i = A_i(Z)/A_i^{st}$  applied to the pre-exponential constants  
667  $A_2$ ,  $A_4$ ,  $A_5$  and  $A_6$  are plotted as function of the mixture fraction in Fig. B1.

## 668 References

## 669 References

- 670 [1] M. Cailler, N. Darabiha, and B. Fiorina, *Development of a virtual optimized chem-*  
671 *istry method. Application to hydrocarbon/air combustion*, Combustion and Flame



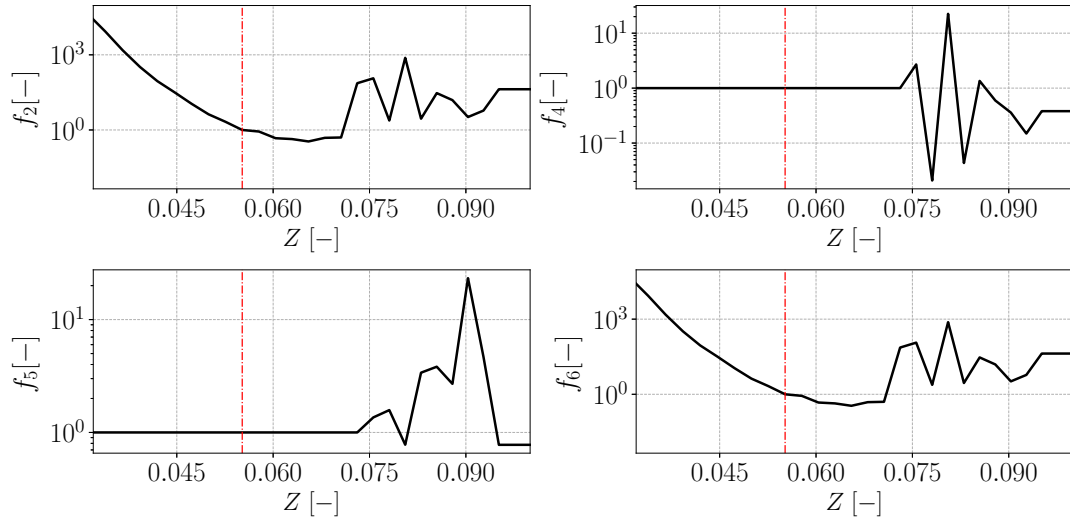


Figure B1.: Correction function  $f_i$  applied to pre-exponential constants  $A_2$ ,  $A_4$ ,  $A_5$  and  $A_6$ , respectively. The stoichiometric mixture fraction is also shown through the vertical line.

- 672 211 (2020), pp. 281–302.
- 673 [2] I.E.A. International Energy Agency, *World energy outlook 2016*,  
674 <https://webstore.iea.org/world-energy-outlook-2016> (2016).
- 675 [3] G.P. Smith, D.M. Golden, M. Frenklach, B. Eiteener, M. Goldenberg, C.T.  
676 Bowman, R.K. Hanson, W.C. Gardiner, V.V. Lissianski, and Z.W. Qin,  
677 [http://www.me.berkeley.edu/gri\\_mech](http://www.me.berkeley.edu/gri_mech) (2011).
- 678 [4] A.H. Lefebvre, *Gas turbine combustion*, CRC press, 1998.
- 679 [5] N. Darabiha, *Transient behaviour of laminar counterflow hydrogen-air diffusion*  
680 *flames with complex chemistry*, *Combust. Sci. Technol.* 86 (1992), pp. 163–181.
- 681 [6] C. Fenimore, *Formation of nitric oxide in premixed hydrocarbon flames*, in *Sym-*  
682 *posium (International) on Combustion*, Vol. 13. Elsevier, 1971, pp. 373–380.
- 683 [7] A. Hayhurst and I. Vince, *Nitric oxide formation from  $N_2$  in flames: the impor-*  
684 *tance of “prompt” NO*, *Progress in Energy and Combustion Science* 6 (1980), pp.  
685 35–51.
- 686 [8] Y.B. Zeldovich, *Selected Works of Yakov Borisovich Zeldovich, Volume I: Chem-*  
687 *ical Physics and Hydrodynamics*, Vol. 140, Princeton University Press, 2014.
- 688 [9] K.K. Kuo, *Principles of combustion*, John Wiley 2005, 2005.
- 689 [10] T. Faravelli, A. Frassoldati, and E. Ranzi, *Kinetic modeling of the interactions be-*  
690 *tween NO and hydrocarbons in the oxidation of hydrocarbons at low temperatures*,  
691 *Combustion and Flame* 132 (2003), pp. 188–207.
- 692 [11] A. Frassoldati, T. Faravelli, and E. Ranzi, *Kinetic modeling of the interactions*  
693 *between NO and hydrocarbons at high temperature*, *Combustion and Flame* 135  
694 (2003), pp. 97–112.
- 695 [12] P. Glarborg, J.A. Miller, B. Ruscic, and S.J. Klippenstein, *Modeling nitrogen*  
696 *chemistry in combustion*, *Progress in Energy and Combustion Science* 67 (2018),  
697 pp. 31–68.
- 698 [13] T. Lu and C.K. Law, *Toward accommodating realistic fuel chemistry in large-*  
699 *scale computations*, *Progress in Energy and Combustion Science* 35 (2009), pp.  
700 192–215.

- 701 [14] H. Wang and M. Frenklach, *Detailed reduction of reaction mechanisms for flame*  
702 *modeling*, Combustion and Flame 87 (1991), pp. 365–370.
- 703 [15] B. Fiorina, D. Veynante, and S. Candel, *Modeling combustion chemistry in large*  
704 *eddy simulation of turbulent flames*, Flow, Turbulence and Combustion 94 (2015),  
705 pp. 3–42.
- 706 [16] B. Fiorina and M. Cailler, *Accounting for complex chemistry in the simulations*  
707 *of future turbulent combustion systems*, in *AIAA Scitech 2019 Forum*. 2019, p.  
708 0995.
- 709 [17] C.K. Westbrook and F.L. Dryer, *Simplified reaction mechanisms for the oxidation*  
710 *of hydrocarbon fuels in flames*, Combustion science and technology 27 (1981), pp.  
711 31–43.
- 712 [18] W. Jones and R. Lindstedt, *Global reaction schemes for hydrocarbon combustion*,  
713 Combustion and flame 73 (1988), pp. 233–249.
- 714 [19] N. Peters, *Laminar diffusion flamelet models in non-premixed turbulent combus-*  
715 *tion*, Progress in energy and combustion science 10 (1984), pp. 319–339.
- 716 [20] O. Gicquel, N. Darabiha, and D. Thévenin, *Laminar premixed hydrogen/air coun-*  
717 *terflow flame simulations using flame prolongation of ILDM with differential dif-*  
718 *fusion*, Proceedings of the Combustion Institute 28 (2000), pp. 1901–1908.
- 719 [21] J. Van Oijen, F. Lammers, and L. De Goey, *Modeling of complex premixed burner*  
720 *systems by using flamelet-generated manifolds*, Combustion and Flame 127 (2001),  
721 pp. 2124–2134.
- 722 [22] T. Lu and C.K. Law, *A criterion based on computational singular perturbation for*  
723 *the identification of quasi steady state species: A reduced mechanism for methane*  
724 *oxidation with NO chemistry*, Combustion and Flame 154 (2008), pp. 761–774.
- 725 [23] P. Pepiot-Desjardins and H. Pitsch, *An efficient error-propagation-based reduction*  
726 *method for large chemical kinetic mechanisms*, Combustion and Flame 154 (2008),  
727 pp. 67–81.
- 728 [24] E. Fernandez-Tarrazo, A.L. Sánchez, A. Linan, and F.A. Williams, *A simple one-*  
729 *step chemistry model for partially premixed hydrocarbon combustion*, Combustion  
730 and Flame 147 (2006), pp. 32–38.
- 731 [25] B. Franzelli, E. Riber, M. Sanjosé, and T. Poinsot, *A two-step chemical scheme for*  
732 *kerosene-air premixed flames*, Combustion and Flame 157 (2010), pp. 1364–1373.
- 733 [26] T. Jaravel, E. Riber, B. Cuenot, and G. Bulat, *Large eddy simulation of an in-*  
734 *dustrial gas turbine combustor using reduced chemistry with accurate pollutant*  
735 *prediction*, Proceedings of the Combustion Institute 36 (2017), pp. 3817–3825.
- 736 [27] T. Jaravel, E. Riber, B. Cuenot, and P. Pepiot, *Prediction of flame structure and*  
737 *pollutant formation of Sandia flame D using large eddy simulation with direct*  
738 *integration of chemical kinetics*, Combustion and Flame 188 (2018), pp. 180–198.
- 739 [28] U. Maas and S.B. Pope, *Implementation of simplified chemical kinetics based on*  
740 *intrinsic low-dimensional manifolds*, in *Symposium (International) on Combus-*  
741 *tion*, Vol. 24. Elsevier, 1992, pp. 103–112.
- 742 [29] V. Bykov and U. Maas, *The extension of the ildm concept to reaction-diffusion*  
743 *manifolds*, Combustion Theory and Modelling 11 (2007), pp. 839–862.
- 744 [30] J. Nafe and U. Maas, *Modeling of NO formation based on ildm reduced chemistry*,  
745 Proceedings of the Combustion Institute 29 (2002), pp. 1379–1385.
- 746 [31] G. Godel, P. Domingo, and L. Vervisch, *Tabulation of NOx chemistry for large-*  
747 *eddy simulation of non-premixed turbulent flames*, Proceedings of the Combustion  
748 Institute 32 (2009), pp. 1555–1561.
- 749 [32] A. Vreman, B. Albrecht, J. Van Oijen, L. De Goey, and R. Bastiaans, *Premixed*  
750 *and nonpremixed generated manifolds in large-eddy simulation of Sandia flame D*

- 751 and *F*, *Combustion and Flame* 153 (2008), pp. 394–416.
- 752 [33] M. Ihme and H. Pitsch, *Modeling of radiation and nitric oxide formation in turbu-*  
753 *lent nonpremixed flames using a flamelet/progress variable formulation*, *Physics*  
754 *of Fluids* 20 (2008), p. 055110.
- 755 [34] A. Ketelheun, C. Olbricht, F. Hahn, and J. Janicka, *No prediction in turbulent*  
756 *flames using LES/FGM with additional transport equations*, *Proceedings of the*  
757 *Combustion Institute* 33 (2011), pp. 2975–2982.
- 758 [35] F. Pecquery, V. Moureau, G. Lartigue, L. Vervisch, and A. Roux, *Modelling ni-*  
759 *trogen oxide emissions in turbulent flames with air dilution: Application to LES*  
760 *of a non-premixed jet-flame*, *Combustion and Flame* 161 (2014), pp. 496–509.
- 761 [36] P.E. Vervisch, O. Colin, J.B. Michel, and N. Darabiha, *NO relaxation approach*  
762 *(NORA) to predict thermal NO in combustion chambers*, *Combustion and Flame*  
763 158 (2011), pp. 1480–1490.
- 764 [37] B. Fiorina, O. Gicquel, L. Vervisch, S. Carpentier, and N. Darabiha, *Approximat-*  
765 *ing the chemical structure of partially premixed and diffusion counterflow flames*  
766 *using FPI flamelet tabulation*, *Combustion and flame* 140 (2005), pp. 147–160.
- 767 [38] P.D. Nguyen, L. Vervisch, V. Subramanian, and P. Domingo, *Multidimensional*  
768 *flamelet-generated manifolds for partially premixed combustion*, *Combustion and*  
769 *Flame* 157 (2010), pp. 43–61.
- 770 [39] V. Bykov and U. Maas, *Problem adapted reduced models based on reaction-*  
771 *diffusion manifolds (REDIMs)*, *Proceedings of the Combustion Institute* 32  
772 (2009), pp. 561–568.
- 773 [40] M. Cailler, N. Darabiha, D. Veynante, and B. Fiorina, *Building-up virtual opti-*  
774 *mized mechanism for flame modeling*, *Proc. Combust. Inst.* (2017).
- 775 [41] G. Maio, M. Cailler, R. Mercier, and B. Fiorina, *Virtual chemistry for temperature*  
776 *and CO prediction in LES of non-adiabatic turbulent flames*, *Proceedings of the*  
777 *Combustion Institute* 37 (2019), pp. 2591–2599.
- 778 [42] A. Cuoci, A. Frassoldati, T. Faravelli, and E. Ranzi, *A computational tool for*  
779 *the detailed kinetic modeling of laminar flames: Application to C<sub>2</sub>H<sub>4</sub>/CH<sub>4</sub> coflow*  
780 *flames*, *Combustion and Flame* 160 (2013), pp. 870–886.
- 781 [43] J. Caudal, B. Fiorina, B. Labergorre, and O. Gicquel, *Modeling interactions be-*  
782 *tween chemistry and turbulence for simulations of partial oxidation processes*,  
783 *Fuel Processing Technology* 134 (2015), pp. 231–242, Available at [http://dx.  
784 doi.org/10.1016/j.fuproc.2015.01.040](http://dx.doi.org/10.1016/j.fuproc.2015.01.040).
- 785 [44] OpenFOAM (2019). Available at [www.openfoam.org](http://www.openfoam.org).
- 786 [45] A. Cuoci, A. Frassoldati, T. Faravelli, and E. Ranzi, *Numerical modeling of lam-*  
787 *inar flames with detailed kinetics based on the operator-splitting method*, *Energy*  
788 *& Fuels* 27 (2013), pp. 7730–7753.
- 789 [46] A. Stagni, A. Cuoci, A. Frassoldati, T. Faravelli, and E. Ranzi, *Lumping and re-*  
790 *duction of detailed kinetic schemes: an effective coupling*, *Industrial & Engineering*  
791 *Chemistry Research* 53 (2013), pp. 9004–9016.
- 792 [47] M.S. Day and J.B. Bell, *Numerical simulation of laminar reacting flows with*  
793 *complex chemistry*, *Combustion Theory and Modelling* 4 (2000), pp. 535–556.
- 794 [48] C.K. Law, *Combustion at a crossroads: Status and prospects*, *Proceedings of the*  
795 *Combustion Institute* 31 (2007), pp. 1–29.
- 796 [49] P. Pepiot, *Automatic strategies to model transportation fuel surrogates*, Stanford  
797 University Stanford, CA, Ph.D thesis, 2008.